

# Learning from geometry-aware near-misses to real-time COR: A spatiotemporal grouped random GEV framework

Mohammad Anis<sup>a</sup>, Yang Zhou<sup>a,\*</sup> and Dominique Lord<sup>a</sup>

<sup>a</sup>Zachry Department of Civil & Environmental Engineering, Texas A&M University, College Station, TX 77843, USA

## ARTICLE INFO

### Keywords:

Corridor-wide crash risk  
Short-term risk prediction  
Near-miss  
2D-TTC  
Extreme value theory  
Hierarchical Bayesian modeling

## ABSTRACT

Real-time corridor-wide crash occurrence risk (COR) prediction is challenging because existing near-miss EVT models oversimplify collision geometry, neglect vehicle–infrastructure (V–I) interactions, and fail to capture spatial heterogeneity in traffic and roadway conditions. To address these gaps, this study introduces a geometry-aware two-dimensional time-to-collision (2D-TTC) indicator for capturing V–V and V–I near misses, and a Hierarchical Bayesian spatiotemporal grouped random parameter (HBSGRP) UGEV model for estimating short-term COR in urban corridors. High-resolution trajectories from the Argoverse-2 dataset were analyzed across 28 sites on Miami’s Biscayne Boulevard to extract extreme near-miss events. The model incorporates vehicle dynamics and roadway features as covariates, with partial pooling across segments and intersections to capture corridor-wide heterogeneity. Results show that the HBSGRP–UGEV framework outperforms fixed-parameter models, reducing DIC by up to 7.5% for V–V and 3.1% for V–I near misses. Predictive validation using ROC–AUC confirms strong accuracy (0.89 for V–V segments, 0.82 for intersections, 0.79 for V–I segments, and 0.75 for intersections). Random-parameter effects showed that relative speed, distance, and deceleration dominated V–V near misses at segments (only distance for V–I), while intersections were dominated by relative speed and distance for V–V, with no significant effects for V–I. These findings demonstrate the value of a geometry-aware, spatially adaptive framework for proactive corridor safety management, supporting both real-time interventions and long-term Vision Zero goals.

## 1. Introduction

The increasing complexity of urban corridors, rising traffic volumes, and the coexistence of human-driven vehicles (HDVs) and autonomous vehicles (AVs) demand innovative safety assessment approaches. Urban corridors are particularly vulnerable, as even a single crash can disrupt mobility, trigger cascading congestion, and result in substantial economic losses. In 2023, traffic crashes in the United States claimed 40901 lives, with a fatality rate of 1.26 per 100 million vehicle miles traveled (VMT) (National Center for Statistics and Analysis, 2025). The total annual cost of crashes exceeds \$1.85 trillion, including \$460 billion in direct economic losses and \$1.4 trillion in reduced quality of life (Blincoe et al., 2023). Despite decades of research, corridor-wide crash risk prediction remains methodologically limited.

Crash risk prediction has traditionally relied on retrospective crash data (Arun et al., 2021; Lee et al., 2017; Pei et al., 2011). While such approaches have advanced understanding of crash patterns, they face well-documented limitations (Lord and Mannering, 2010; Lord et al., 2021; Mannering et al., 2020), including the rarity and stochastic nature of crashes, underreporting (Arun et al., 2021; Tarko, 2018), temporal delays, and spatial mismatches with real-time traffic conditions. These drawbacks highlight the need for proactive approaches that anticipate rather than react to crash risk.

To address these challenges, researchers have shifted toward proactive trajectory-based surrogate safety measures (SSMs) (Ali et al., 2023a; Arun et al., 2021; Mahmud et al., 2017). SSMs use frequent near-miss events as proxies for crashes, enabling the study of traffic conflict dynamics at a much higher temporal resolution (Li et al., 2024; Tarko, 2018; Davis et al., 2011). Among these, time-based indicators such as Time-to-Collision (TTC), Post-Encroachment Time (PET), and Modified TTC (MTTC) are widely used (Hayward, 1971; Perkins and Harris, 1967; Minderhoud and Bovy, 2001; Ozbay et al., 2008; Allen et al., 1978; Venthuruthiyil and Chunchu, 2022). However, their assumptions of constant velocity and linear paths bias results in boundary-constrained settings. Recent two-dimensional (2D) extensions (Li et al., 2024; Anis et al., 2025b) incorporate position, heading, and acceleration, yet still rely on simplified

\*Corresponding author

 yangzhou295@tamu.edu (Yang Zhou)

circular vehicle approximations. This study addresses these limitations by introducing a geometry-aware 2D-TTC that accounts for vehicle dimensions, dynamics, and roadway boundaries to realistically capture both vehicle–vehicle (V–V) and vehicle–infrastructure (V–I) near misses.

Building on this foundation, recent studies have integrated SSMs with extreme value theory (EVT) to estimate crash occurrence risk (COR) in urban corridors (Lanzaro et al., 2023; Kamel et al., 2023, 2024; Kamel and Sayed, 2024; Singh et al., 2024; Ghoual and Sayed, 2025; Singh et al., 2025; Anis et al., 2025b). EVT extrapolates from frequent near misses to rare crash-prone extremes, offering a statistically principled framework for proactive safety analysis. Yet most SSM–EVT applications remain limited, focusing narrowly on V–V interactions and excluding V–I conflicts such as lane edges, curbs, and barriers. This omission is critical because V–I events account for a large share of severe roadway departure crashes (Islam et al., 2021). Recent advances in AV sensing and high-definition (HD) mapping, such as the Argoverse-2 dataset (Wilson et al., 2023), now enable precise alignment of roadway boundaries with vehicle trajectories, creating new opportunities to model both V–V and V–I near misses with geometric fidelity.

While SSMs capture frequent near misses, robust COR estimation requires extrapolating extreme near misses to rare crash outcomes. EVT (Fu and Sayed, 2021a,b; Zheng et al., 2021b; Ali et al., 2023a; Zheng et al., 2021a; Songchitruksa and Tarko, 2006; Zheng et al., 2014; Tarko, 2012) has become the most widely used method for this task, with two dominant formulations: the Generalized Extreme Value (GEV) distribution using Block Maxima (BM) sampling, and the Generalized Pareto Distribution (GPD) using Peaks-over-Threshold (POT) sampling (Coles et al., 2001). The BM approach is particularly well-suited to real-time applications due to its short block structure, reduced threshold sensitivity, and compatibility with discrete-time samples (Fu and Sayed, 2022a).

Early applications of EVT in traffic safety used stationary GEV models (Wang et al., 2018; Guo et al., 2019; Orsini et al., 2019; Alozi and Hussein, 2022; Hussain et al., 2022), which assumed constant parameters across study areas. More recent work has developed nonstationary GEV formulations, allowing covariates to influence distribution parameters (Tahir and Haque, 2024; Ali et al., 2022; Fu and Sayed, 2022a; Zheng et al., 2019; Nazir et al., 2023; Kar et al., 2024; Ali et al., 2023b; Alozi and Hussein, 2022; Zheng et al., 2014; Kar et al., 2023) and capture heterogeneity across traffic states. (Lanzaro et al., 2023; Kamel et al., 2023, 2024; Kamel and Sayed, 2024; Singh et al., 2024; Ghoual and Sayed, 2025; Singh et al., 2025; Anis et al., 2025b). Bayesian hierarchical extensions further address data sparsity and unobserved heterogeneity (Zheng and Sayed, 2019; Fu and Sayed, 2022b). Despite these advances, most applications remain geographically narrow and functionally restricted to either intersections (Fu and Sayed, 2023, 2021c, 2022b) or segments (Kumar and Mudgal, 2024; Kamel et al., 2023; Kamel and Sayed, 2024; Anis et al., 2025b; Kamel et al., 2024). Although some studies have integrated vehicle dynamics (Kumar and Mudgal, 2024; Fu and Sayed, 2022b; Anis et al., 2025b) and examined heterogeneity across traffic flow directions or roadway geometries (Kamel et al., 2023, 2024), explicit corridor-wide models that jointly integrate vehicle dynamics, roadway geometry, and directional heterogeneity remain rare.

To address this gap, this paper makes three contributions: (1) it develops a corridor-wide COR framework that incorporates both V–V and V–I interactions, (2) it introduces a geometry-aware 2D-TTC indicator that captures extreme near-miss dynamics with higher geometric fidelity, and (3) it advances a hierarchical Bayesian spatiotemporal grouped random parameter (HBSGRP) GEV model that integrates roadway geometry, traffic directionality, and multilevel heterogeneity for corridor-wide yet location-sensitive crash risk estimation.

Together, these contributions establish the first infrastructure-aware, statistically rigorous framework for proactive corridor-wide crash risk prediction, leveraging Argoverse-2 trajectory and HD map data to support both real-time interventions and long-term safety planning.

The remainder of this paper introduces the proposed 2D-TTC indicators, the HBSGRP–UGEV modeling framework, and the data preparation used in the analysis. This is followed by the presentation of model estimation, validation, and comparative results. The paper concludes with key findings, limitations, and directions for future research.

## 2. Near-miss detection framework

This section presents the modeling framework for computing a geometry-aware, high-fidelity 2D-TTC to support COR estimation. The framework integrates a continuous-time kinematic bicycle model, vehicle geometry representation, and a spatial near-miss detection algorithm, allowing capture of V–V and V–I interactions. Together, these components enable the accurate forecasting of vehicle trajectories and identification of potential near misses. The resulting architecture forms the computational backbone of the SSM analysis, ensuring a realistic representation of near-miss events in mixed-traffic environments.

## 2.1. Vehicle dynamics model

The vehicle dynamics module provides the predictive foundation of the framework. This adopts the kinematic bicycle model to represent vehicle footprint, as it is suitable for short-term near-miss analysis, where steering and acceleration dominate, and lateral slip can be neglected. The motion is represented by a four-dimensional (4D) dynamic state vector. At any time  $t$ , the state of vehicle  $i$  is given by:

$$\mathbf{x}_i(t) = \begin{bmatrix} x_i(t) \\ y_i(t) \\ \theta_i(t) \\ v_i(t) \end{bmatrix} \quad (1)$$

Here,  $x_i(t)$ ,  $y_i(t)$  denote the vehicle's global center coordinates,  $\theta_i(t)$  its heading angle, and  $v_i(t)$  its speed. Over the prediction window, each vehicle is assumed to maintain constant acceleration  $a_i$  and steering angle  $\delta_i$ , simplifying short-horizon trajectory integration. The motion then follows the standard kinematic bicycle equations:

$$\dot{x}_i(t) = v_i(t) \cos \theta_i(t) \quad (2)$$

$$\dot{y}_i(t) = v_i(t) \sin \theta_i(t) \quad (3)$$

$$\dot{\theta}_i(t) = \frac{v_i(t)}{L_i} \tan \delta_i \quad (4)$$

$$\dot{v}_i(t) = a_i \quad (5)$$

Here,  $L_i$  is the vehicle wheelbase, influencing the turning radius and path curvature of vehicle  $i$ . The steering angle  $\delta_i$  and acceleration  $a_i$  are treated as fixed inputs over the lookahead period. Equations (2-5) describe the rates of change in position, orientation, and velocity, determining the vehicle's trajectory. To model interactions, individual states are concatenated into an eight-dimensional (8D) joint state vector, defined as:

$$X(t) = \left[ x_A(t) \quad y_A(t) \quad \theta_A(t) \quad v_A(t) \quad x_B(t) \quad y_B(t) \quad \theta_B(t) \quad v_B(t) \right]^T \quad (6)$$

The vector field that governs the evolution of this combined state is  $F$  defined as:

$$\dot{X}(t) = F(X(t)) = \left[ v_A \cos \theta_A \quad v_A \sin \theta_A \quad \frac{v_A}{L_A} \tan \delta_A \quad a_A \quad v_B \cos \theta_B \quad v_B \sin \theta_B \quad \frac{v_B}{L_B} \tan \delta_B \quad a_B \right]^T \quad (7)$$

The state-space vector field in Eqn.7 gives the instantaneous rate of change of the joint state  $\dot{X}(t)$ . Its forward evolution is computed using the fourth-order Runge–Kutta (RK4) method, which balances accuracy and efficiency for nonlinear vehicle dynamics. The time horizon is discretized into  $N$  steps of size  $\Delta t$  ( $t_n = n\Delta t$ ,  $n = 0, 1, \dots, N$ ), and the RK4 update for state  $X(t_{n+1})$  from  $X(t_n)$  is:

$$X_{n+1} = X_n + \frac{\Delta t}{6} (k_1 + 2k_2 + 2k_3 + k_4) \quad (8)$$

where the intermediate slope evaluations  $k_1, \dots, k_4 \in \mathbb{R}^8$  are defined as:

$$k_1 = F(X_n)$$

$$k_2 = F\left(X_n + \frac{\Delta t}{2} k_1\right)$$

$$\begin{aligned}
k_3 &= F \left( X_n + \frac{\Delta t}{2} k_2 \right) \\
k_4 &= F \left( X_n + \Delta t \cdot k_3 \right)
\end{aligned} \tag{9}$$

This integration is repeated for each timestep  $n \in \{0, \dots, N - 1\}$ , producing a sequence of predicted states  $\{X_n\}$  over the horizon. These trajectories form the basis for geometric collision checks between vehicles and roadway boundaries.

## 2.2. Vehicle geometry representation

Although the dynamic model predicts vehicle positions and headings, accurate near-miss detection requires a realistic representation of the vehicle footprint. Simplifying vehicles as points or circles often misrepresents interactions, especially during lane changes, swerving, or angled approaches. To address this, each vehicle is modeled as a rigid rectangle defined by its actual length  $L_i^{\text{veh}}$  and width  $W_i^{\text{veh}}$  (vehicle  $i \in \{A, B\}$ ). The vehicle is centered at its center of gravity, with four corners specified in the body-fixed coordinate system as:

$$b_i^{(j)} = \begin{bmatrix} \xi_i^{(j)} \\ \eta_i^{(j)} \end{bmatrix}, \quad j = 1, 2, 3, 4 \tag{10}$$

where  $\xi_i^{(j)} \in \left\{ +\frac{L_i^{\text{veh}}}{2}, -\frac{L_i^{\text{veh}}}{2} \right\}$  and  $\eta_i^{(j)} \in \left\{ +\frac{W_i^{\text{veh}}}{2}, -\frac{W_i^{\text{veh}}}{2} \right\}$ . This results in four corners: front-left, front-right, rear-left, and rear-right, expressed relative to the vehicle's center in the local frame.

To compute the position of each corner in the global coordinate frame at time  $t$ , the body-fixed corner coordinates are first rotated by the vehicle's heading angle  $\theta_i(t)$ , and then translated by the vehicle's center position  $(x_i(t), y_i(t))$ . This transformation is written as:

$$p_i^{(j)}(t) = \begin{bmatrix} x_i(t) \\ y_i(t) \end{bmatrix} + R(\theta_i(t)) \cdot b_i^{(j)} \tag{11}$$

where  $R(\theta_i(t))$  is the 2D rotation matrix defined as:

$$R(\theta_i(t)) = \begin{bmatrix} \cos \theta_i(t) & -\sin \theta_i(t) \\ \sin \theta_i(t) & \cos \theta_i(t) \end{bmatrix} \tag{12}$$

This transformation rotates the local corner coordinates by the heading angle and translates them into the global frame. Repeating it for all corners at each timestep produces the vehicle's time-varying geometric footprint, which serves as input for near-miss detection. These footprints enable precise evaluation of proximity-based events, both V-V and V-I, ensuring accurate 2D-TTC estimation while reducing false positives from geometric simplifications.

## 2.3. V-V near-miss detection

Vehicles are modeled as rigid rectangles, and their interactions are determined by predicted states and orientations. At each timestep of the RK4 integration, the global positions of all four corners are computed using the kinematic and rotational transformations. A collision is defined when a vehicle's corner lies within a proximity threshold of a corner of another vehicle. Let  $p_A^{(j)}(t)$  and  $p_B^{(k)}(t)$  denote the global coordinates of corners  $j$  and  $k$  of vehicles A and B at time  $t$ . A V-V near-miss is flagged if any pair of these corners satisfies the proximity condition.

$$p_A^{(j)}(t) = p_B^{(k)}(t) \tag{13}$$

An exact match between corners of two vehicles is highly unlikely due to floating-point arithmetic and continuous motion. Instead, a practical criterion is applied: a collision is flagged if the difference in both the x and y coordinates of any corner pair is less than or equal to a small threshold  $\epsilon$ :

$$|x_A^{(j)} - x_B^{(k)}| \leq \varepsilon \quad (14)$$

$$|y_A^{(j)} - y_B^{(k)}| \leq \varepsilon \quad (15)$$

The rotation–translation transformation from each vehicle’s center and heading angle gives the global corner coordinates, for vehicles  $A$  and  $B$ :

$$x_A^{(j)} = x_A + \xi_A^{(j)} \cos \theta_A - \eta_A^{(j)} \sin \theta_A \quad (16)$$

$$y_A^{(j)} = y_A + \xi_A^{(j)} \sin \theta_A + \eta_A^{(j)} \cos \theta_A \quad (17)$$

$$x_B^{(k)} = x_B + \xi_B^{(k)} \cos \theta_B - \eta_B^{(k)} \sin \theta_B \quad (18)$$

$$y_B^{(k)} = y_B + \xi_B^{(k)} \sin \theta_B + \eta_B^{(k)} \cos \theta_B \quad (19)$$

At each timestep, all 16 corner-pair combinations are evaluated. A V–V near-miss is flagged if any pair satisfies the proximity condition, and the corresponding collision time  $t_c$  is recorded for 2D-TTC computation. This discrete-time approach enables accurate detection of spatial overlap while avoiding the oversimplifications of circular vehicle approximations.

## 2.4. V-I near-miss detection

In addition to V–V interactions, the framework also detects near misses between vehicles and roadway infrastructure, including curbs, medians, or barriers. Capturing these V–I events is critical for identifying edge encroachments or departures that often precede run-off-road crashes.

Road boundaries are represented as static polylines of  $M$  discrete points  $(X_\ell, Y_\ell)$  consistent with HD map formats in datasets such as Argoverse-2. At each timestep, the global positions of the four vehicle corners  $p_i^{(j)}(t)$  are obtained from the predicted state. The distance between a vehicle corner  $j$  and boundary point  $\ell$ , the distance at time  $t$  is computed as:

$$d_{j,\ell}(t) = \sqrt{(x^{(j)}(t) - X_\ell)^2 + (y^{(j)}(t) - Y_\ell)^2} \quad (20)$$

A near-miss is flagged if  $d_{j,\ell}(t) \leq \varepsilon$  for any corner and boundary point, where  $\varepsilon$  is a proximity threshold accounting for numerical tolerances. When this occurs, the corresponding time  $t_c$  is recorded as the instant of boundary contact. These events are then passed to the 2D-TTC framework to support extreme risk estimation.

## 2.5. Spatiotemporal COR

The near-miss detection framework integrates vehicle dynamics, geometric transformations, and spatial proximity checks to identify both V–V and V–I events. Forward trajectories are simulated using RK4 integration, vehicle corners are transformed into global coordinates, and geometric overlaps are evaluated to detect potential near-misses across the prediction horizon. The procedure is summarized in Algorithm 1, and a conceptual illustration is provided in Fig. 1. These steps yield a time series of 2D-TTC values for each interaction block.

While this geometric framework enables precise localization of near misses, it does not capture the probabilistic structure or temporal evolution of COR. To address this, the extracted blockwise minima of 2D-TTC are modeled using the EVT model. For each block, the model estimates the probability that 2D-TTC falls below a critical safety threshold, which defines the COR metric as a short-term indicator of crash risk. Block duration is chosen to balance temporal sensitivity with statistical stability across diverse contexts. This framework, therefore, combines deterministic near-miss detection with probabilistic EVT modeling to enable localized, data-driven assessment of crash-prone conditions. The complete methodological pipeline, from trajectory simulation to dynamic risk estimation, is summarized in Fig. 2.

## 3. Extreme value theory (EVT)

Extreme Value Theory (EVT) provides the statistical foundation for estimating COR by extrapolating rare, high-severity events from frequent near-misses. In this study, extreme events are represented by block maxima of 2D-TTC derived from high-resolution vehicle trajectories (Algorithm 1). EVT allows risk estimation without requiring

---

**Algorithm 1:** Near-miss detection based on state integration and geometric overlap

---

**Input:** Initial state  $\mathbf{X}(0)$ , vehicle parameters  $l_i, L_i^{\text{veh}}, W_i^{\text{veh}}$ , control inputs  $a_i, \delta_i$ , and boundary points  $\{(X_\ell, Y_\ell)\}$

**Output:** Earliest collision time  $t_c$

```
1 for each timestep  $n = 0$  to  $N - 1$  do
2   Simulate  $\mathbf{X}_n \rightarrow \mathbf{X}_{n+1}$  using RK4 integration;
3   Compute global corner positions  $\mathbf{p}_i^{(j)}$  for each vehicle;
4   for each corner pair  $(j, k) \in \{1, 2, 3, 4\}^2$  do
5     if  $|x_A^{(j)} - x_B^{(k)}| \leq \varepsilon$  or  $|y_A^{(j)} - y_B^{(k)}| \leq \varepsilon$  then
6       Record V-V near-miss, set  $t_c$ ;
7   for each corner  $j$  and boundary point  $\ell$  do
8     Compute  $d_{j,\ell}(t) = \sqrt{(x^{(j)} - X_\ell)^2 + (y^{(j)} - Y_\ell)^2}$ ;
9     if  $d_{j,\ell}(t) \leq \varepsilon$  then
10      Record V-I near-miss, set  $t_c$ ;
11 return the earliest collision time  $t_c$  as 2D-TTC
```

---

large volumes of historical crash data (Zheng and Sayed, 2020; Fu and Sayed, 2022a). Two EVT approaches are commonly applied: the Block Maxima (BM) method, which fits maxima or minima from fixed-duration blocks using the Generalized Extreme Value (GEV) distribution (Coles et al., 2001), and the Peaks Over Threshold (POT) method, which models threshold exceedances using the Generalized Pareto Distribution (GPD). Although POT can be data-efficient, it is highly sensitive to threshold choice and less compatible with discrete sensor-derived datasets. By contrast, BM aligns naturally with real-time AV data, avoids subjective thresholds, and supports scalable, time-series analysis (Fu and Sayed, 2022a; Songchitruksa and Tarko, 2006). Consequently, this study adopts the BM–GEV framework (see Fig. 2).

The GEV has been widely applied in traffic safety research. Early studies modeled near-misses with univariate and multivariate GEV formulations (Orsini et al., 2020; Zhang et al., 2019; Zheng et al., 2014). Recent advances incorporate nonstationary structures, linking GEV parameters to covariates such as vehicle dynamics (Anis et al., 2025b; Fu and Sayed, 2021c, 2022b). Bayesian hierarchical models have also addressed sparse data and unobserved heterogeneity across vehicles, sites, and traffic contexts. The increasing availability of high-resolution AV trajectory and HD map data has highlighted the need for flexible GEV formulations that jointly capture V–V and V–I interactions.

Despite this progress, most UGEV models still neglect the joint influence of roadway geometry and vehicle dynamics, two critical but distinct sources of heterogeneity. Roadway geometry (e.g., lane count, curvature, median type) is spatially structured and relatively stable within segments or intersections, while vehicle dynamics (e.g., speed, acceleration) vary temporally and spatially, driving short-term behavioral volatility. Capturing this multilevel heterogeneity is crucial for estimating corridor and network level crash risk. To address this gap, this study develops a hierarchical Bayesian Spatiotemporal Grouped Random Parameter (HBSGRP) UGEV model. Unlike standard random-parameter models, which assign variation independently to each unit, grouped random parameters capture shared variation across clusters (e.g., segment types, corridor directions) while allowing for within-group variability. This structure provides both flexibility and parsimony, making it well-suited for high-resolution, corridor-scale crash risk modeling (Washington et al., 2020; Cai et al., 2018; Islam et al., 2023).

### 3.1. Univariate generalized extreme value (UGEV)

As established in the previous section, the BM-based UGEV model is employed to characterize the tail behavior of 2D-TTC, which represents the most critical near-miss events in both V–V and V–I interactions. To implement this framework, continuous vehicle trajectories are partitioned into fixed-duration windows (e.g., 11 s). Within each window, the minimum 2D-TTC is extracted and negated, consistent with the upper-tail modeling convention of UGEV (Coles et al., 2001). The resulting sequence of BM serves as the input for parameter estimation. Throughout this study, we focus on maxima, denoted as  $M_n$ , under the assumption that each block consists of  $n$  independent and identically distributed (i.i.d.) random variables,  $X_1, X_2, \dots, X_n$ . To align with conventional UGEV formulations, we

consider the negative values of the original variables derived from Algorithm 1, thereby defining the block maximum as  $M_n = \max\{-X_1, -X_2, \dots, -X_n\}$ . Under suitable regularity conditions, if there exist sequences of constants  $a_n \in \mathbb{R}$  and  $b_n > 0$ , the normalized block maxima  $M_n^* = (M_n - a_n)/b_n$  converge in distribution to a non-degenerate limit  $G(x)$  as  $n \rightarrow \infty$ , then:  $\Pr\left(\frac{M_n - a_n}{b_n} \leq X\right) \xrightarrow{n \rightarrow \infty} f(x)$ , where  $G(x)$  is a non-degenerate distribution function. According to EVT, the limiting distribution  $G(x)$  must belong to one of three families: Gumbel, Fréchet, or Weibull, each of which can be captured by the parametric form of the GEV distribution (Coles et al., 2001). Let the UGEV be defined as:

$$G(x; \mu_x, \sigma_x, \xi_x) = \exp\left\{-\left[1 + \xi_x \left(\frac{x - \mu_x}{\sigma_x}\right)\right]^{-1/\xi_x}\right\}, \quad \text{where } 1 + \xi_x \left(\frac{x - \mu_x}{\sigma_x}\right) > 0 \quad (21)$$

Here,  $\mu_x \in \mathbb{R}$  is the location parameter,  $\sigma_x > 0$  the scale, and  $\xi_x \in \mathbb{R}$  the shape. The value of  $\xi_x$  determines tail heaviness:  $\xi_x > 0$  corresponds to the heavy-tailed Fréchet,  $\xi_x < 0$  to the bounded Weibull, and  $\xi_x = 0$  to the light-tailed Gumbel case.

### 3.1.1. Hierarchical Bayesian Spatiotemporal Grouped Random Parameter (HBSGRP) model

To capture structured heterogeneity in extreme outcomes across the corridor, we employ a Hierarchical Bayesian Spatiotemporal Grouped Random Parameter (HBSGRP) model. Unlike conventional random-parameter models that assign variation to individual units, the HBSGRP formulation introduces variation at the group level. This structure allows systematic differences across predefined observational groups while maintaining parsimony and interpretability. In this specification, covariates are divided into two sets: fixed effects  $X$ , which apply uniformly across all observations, and group-varying effects  $Z$ , whose coefficients differ across groups. For a dataset divided into  $K$  groups, with observations  $i$  belonging to group  $k(i)$ , both the intercept and selected slopes are allowed to vary by group. This enables the capture of localized relationships while preserving overall model coherence. The model is expressed within a three-layer hierarchical Bayesian framework. The data layer specifies the likelihood of observed block maxima of 2D-TTC from V–V and V–I interactions, assuming a UGEV distribution. The process layer links covariates to UGEV parameters through fixed and group-level random effects, with optional latent terms (e.g., Gaussian processes) to capture residual spatial–temporal dependence. The prior layer defines prior distributions for all parameters and hyperparameters, supporting regularization and uncertainty quantification.

Bayesian inference proceeds by updating prior beliefs with observed data to obtain the posterior distribution. Formally, the joint posterior of parameters  $\Theta$ , given data  $X$ , is:

$$q(\Theta | X) \propto q_{\text{data}}(X | \Theta) \cdot q_{\text{process}}(\Theta | \Psi) \cdot q_{\text{prior}}(\Psi) \quad (22)$$

In this formulation,  $q(\Theta | X)$  denotes the posterior distribution, integrating both the data likelihood and prior knowledge. The term  $q_{\text{data}}(X | \Theta)$  corresponds to the likelihood function defined by the EVT assumptions. The component  $q_{\text{process}}(\Theta | \Psi)$  captures the hierarchical dependency structure, including the group-varying parameters. Lastly,  $q_{\text{prior}}(\Psi)$  encompasses the prior distributions of hyperparameters that control the model's flexibility and penalize over-complexity.

The likelihood function for the data layer is specified as each extreme value sample  $X_{k,i}$ , observed for event  $i$  within group  $K$ , is modeled as:

$$q_{\text{data}}(X_{k,i} | \Theta) = \prod_{k=1}^K \prod_{i=1}^{N_k} \frac{1}{\sigma_{k,i}} \exp\left\{-\left[1 + \xi_{k,i} \left(\frac{X_{k,i} - \mu_{k,i}}{\sigma_{k,i}}\right)\right]^{-1/\xi_{k,i}}\right\} \left[1 + \xi_{k,i} \left(\frac{X_{k,i} - \mu_{k,i}}{\sigma_{k,i}}\right)\right]^{-1-1/\xi_{k,i}} \quad (23)$$

The location ( $\mu_{k,i}$ ), scale ( $\sigma_{k,i}$ ), and shape ( $\xi_{k,i}$ ) parameters are expressed as functions of group-level fixed-effect covariates  $X_{k,j}$  (e.g., road geometry, speed limit) and sample-specific random-effect covariates  $W_{k,i,j}$  (e.g., speed, acceleration, time-to-collision) as follows:

$$\mu_{k,i} = \beta_{\mu,0} + \sum_{j=1}^J \beta_{\mu,j} X_{k,j} + \sum_{j=1}^{J'} \gamma_{\mu,j,k} W_{k,i,j} \quad (24)$$

$$\vartheta_{k,i} = \beta_{\sigma,0} + \sum_{j=1}^J \beta_{\sigma,j} X_{k,j} + \sum_{j=1}^{J'} \gamma_{\sigma,j,k} W_{k,i,j}, \quad \sigma_{k,i} = \exp(\vartheta_{k,i}) \quad (25)$$

$$\xi_{k,i} = \beta_{\xi,0} + \sum_{j=1}^J \beta_{\xi,j} X_{k,j} \quad (26)$$

In the above equations,  $X_{k,j}$  defined as a group-level fixed-effect covariate  $j$ ,  $W_{k,i,j}$  is a sample-specific random-effect covariate  $j$ .  $\beta_{\mu,0}$ ,  $\beta_{\sigma,0}$ ,  $\beta_{\xi,0}$  as fixed intercepts for respective parameters.  $\beta_{\mu,j}$ ,  $\beta_{\sigma,j}$ ,  $\beta_{\xi,j}$ : fixed-effect coefficients.  $\gamma_{\mu,j,k}$ ,  $\gamma_{\sigma,j,k}$ : random-effect coefficients, varying across groups  $k$ . Therefore, the likelihood for the process layer, modeling within-group variability, is defined as:

$$q_{\text{process}}(\Theta | \Psi) = \prod_{k=1}^K \prod_{i=1}^{N_k} \frac{1}{\sqrt{2\pi\tau_{\mu}^2}} \exp \left\{ -\frac{1}{2\tau_{\mu}^2} (\mu_{k,i} - \bar{\mu}_k)^2 \right\} \\ \times \frac{1}{\sqrt{2\pi\tau_{\vartheta}^2}} \exp \left\{ -\frac{1}{2\tau_{\vartheta}^2} (\vartheta_{k,i} - \bar{\vartheta}_k)^2 \right\} \times \frac{1}{\sqrt{2\pi\tau_{\xi}^2}} \exp \left\{ -\frac{1}{2\tau_{\xi}^2} (\xi_{k,i} - \bar{\xi}_k)^2 \right\} \quad (27)$$

where  $\bar{\mu}_k$ ,  $\bar{\vartheta}_k$ , and  $\bar{\xi}_k$  are group-specific average parameters.

Prior distributions are assigned to all model parameters. The priors for fixed and random effect coefficients are as follows:

$$q_{\text{prior}}(\Psi) = q_{\beta_{\mu,0}}(\beta_{\mu,0}) \cdot \prod_{j=1}^J q_{\beta_{\mu,j}}(\beta_{\mu,j}) \cdot \prod_{k=1}^K \prod_{j=1}^{J'} q_{\gamma_{\mu,j,k}}(\gamma_{\mu,j,k}) \\ \times q_{\beta_{\sigma,0}}(\beta_{\sigma,0}) \cdot \prod_{j=1}^J q_{\beta_{\sigma,j}}(\beta_{\sigma,j}) \cdot \prod_{k=1}^K \prod_{j=1}^{J'} q_{\gamma_{\sigma,j,k}}(\gamma_{\sigma,j,k}) \times q_{\beta_{\xi,0}}(\beta_{\xi,0}) \cdot \prod_{j=1}^J q_{\beta_{\xi,j}}(\beta_{\xi,j}) \quad (28)$$

Hyperpriors for the variance parameters  $\tau_{\mu}^2$ ,  $\tau_{\vartheta}^2$ ,  $\tau_{\xi}^2$  are modeled using inverse gamma distributions:

$$\tau_{\mu}^2 \sim \text{IG}(\alpha_{\mu}, \beta_{\mu}), \quad \tau_{\vartheta}^2 \sim \text{IG}(\alpha_{\vartheta}, \beta_{\vartheta}), \quad \tau_{\xi}^2 \sim \text{IG}(\alpha_{\xi}, \beta_{\xi}) \quad (29)$$

where  $\text{IG}(\alpha, \beta)$  denotes an inverse gamma prior distribution ensuring positivity constraints for variance parameters.

### 3.2. COR estimation

Building on the HBSGRP-UGEV estimates, the framework computes COR by evaluating the probability that 2D-TTC for both V-V and V-I interactions falls below a critical threshold within each block. Unlike severity-stratified approaches, this framework estimates the total number of latent extreme near-miss events regardless of outcome severity, allowing for a holistic assessment of potential COR under mixed traffic conditions.

Let  $k, i$  denote the block  $i$  within the group  $k$ , where groups correspond to spatial or functional corridor classifications (e.g., intersections or directional segments). The minimum 2D-TTC in each block is modeled with the HBSGRP-UGEV distribution, parameterized by  $\mu_{k,i}$ ,  $\sigma_{k,i}$ , and  $\xi_{k,i}$ . Let  $\omega$  be the critical 2D-TTC threshold below which a near-miss is considered crash-prone. The probability of a crash-level event in block  $i$  of group  $k$  is:

$$P_{k,i}^{\text{crash}} = \Pr(2D-TTC_{k,i} \leq \omega) = 1 - \exp \left\{ - \left[ 1 - \xi_{k,i} \left( \frac{\omega - \mu_{k,i}}{\sigma_{k,i}} \right) \right]^{-1/\xi_{k,i}} \right\}, \quad \text{where } 1 - \xi_{k,i} \left( \frac{\omega - \mu_{k,i}}{\sigma_{k,i}} \right) > 0 \quad (30)$$

Assuming a homogeneous Poisson process for exceedances, the expected COR for the group  $k$  is obtained by aggregating exceedance probabilities across blocks and normalizing by exposure duration  $T$ . Here  $y_{k,i}$  is the number of near-misses (V-V or V-I) in block  $i$ , and  $N_k$  the number of blocks in group  $k$ . The expected COR for group  $k$  is:

$$COR_k = \frac{1}{T} \sum_{i=1}^{N_k} y_{k,i} \cdot P_{k,i}^{\text{crash}} = \frac{1}{T} \sum_{i=1}^{N_k} y_{k,i} \cdot \left[ 1 - \exp \left\{ - \left[ 1 - \xi_{k,i} \left( \frac{\omega - \mu_{k,i}}{\sigma_{k,i}} \right) \right]^{-1/\xi_{k,i}} \right\} \right] \quad (31)$$

The total expected crash frequency across the study area is then:

$$C_{F_{\text{total}}} = \sum_{k=1}^K COR_k = \frac{1}{T} \sum_{k=1}^K \sum_{i=1}^{N_k} y_{k,i} \cdot \left[ 1 - \exp \left\{ - \left[ 1 + \xi_{k,i} \left( \frac{\omega - \mu_{k,i}}{\sigma_{k,i}} \right) \right]^{-1/\xi_{k,i}} \right\} \right] \quad (32)$$

This formulation integrates exceedance probabilities from the HBSGRP-UGEV model with observed V-V and V-I near-miss counts, maintaining a direct link between real-world interaction intensity and modeled crash propensity. By separating probability from exposure, the framework yields interpretable, proactive crash frequency estimates aligned with EVT-based safety assessment.

## 4. Data description

The effectiveness of real-time COR estimation is critically dependent on the fidelity and coverage of trajectory data. Traditional sensing technologies, such as roadside cameras, loop detectors, and fixed LiDAR, have supported safety analysis by capturing speed, spacing, and acceleration patterns (Islam et al., 2021; Yuan et al., 2019; Li et al., 2020). However, these systems suffer from narrow fields of view, occlusion, overlapping detections, and high maintenance costs, which limit scalability and data quality (St-Aubin et al., 2013). Recent advances in AV sensing offer a promising alternative. AV datasets provide high-frequency, multimodal trajectories with unprecedented spatial precision, allowing for detailed analysis of kinematics, spacing, and maneuvers. This richness allows for realistic near-miss detection in complex traffic environments. Despite this potential, AV data remain underutilized in generalized frameworks for real-time COR estimation. For example, studies using the Waymo Open Dataset have focused mainly on localized near-miss events without incorporating roadway geometry or V-I interactions, limiting broader applicability (Anis et al., 2025b).

To address these challenges, this study uses the Argoverse-2 dataset (Wilson et al., 2023), which was collected in 2021 across six U.S. cities (Austin, Detroit, Miami, Palo Alto, Pittsburgh, and D.C.) using SAE Level 4 AVs. Argoverse-2 comprises more than 250k driving scenarios that span 113 roadway segments, with each 11-second scenario sampled at 10 Hz. Compared to Waymo Open (Ettinger et al., 2021), Lyft Level-5 (Houston et al., 2021), and nuScenes (Caesar et al., 2020), Argoverse-2 is uniquely curated to emphasize safety-critical interactions, such as intersection near-misses, lane changes, and pedestrian crossings, conditions most indicative of crash risk. A defining feature of Argoverse-2 is its scene-adaptive sampling, which prioritizes high-interaction episodes rather than routine free-flow traffic. Scenarios are annotated with agent IDs, AV driving mode, and map-relative lane-following behaviors. The sensor suite comprises seven ring cameras and two front-facing stereo cameras (20 Hz), supported by dual 64-beam VLP-32C LiDAR sensors, which produce 107k 3D points per frame. HD maps contain lane centerlines, crosswalks, medians, and drivable areas registered to local coordinates.

Argoverse-2 was selected after benchmarking open-source AV datasets (Table 1). Waymo Open offers a greater total mileage but lower near-miss density and no AV-behavior labels. Lyft Level-5 is confined to a single city and lacks scene-level filtering. nuScenes samples at 2 Hz, limiting the capture of rapid interactions. In contrast, Argoverse-2 balances spatial coverage, sensor fidelity, near-miss-rich scenarios, and behavioral annotations, making it well-suited to this study's goals. This study used motion-forecasting and HD-map modules of Argoverse-2 to extract vehicle trajectories, compute near-miss indicators, and encode roadway geometry.

### 4.1. Data Preprocessing

To operationalize the proposed framework, both the motion forecasting and HD map modules of the Argoverse-2 dataset were processed through a structured pipeline. The preprocessing consisted of four key stages: (i) extraction of multi-agent trajectories, (ii) transformation of coordinates from local map space to global geographic space, (iii) integration with HD map features to contextualize V-I interactions, and (iv) selection of a high-risk urban corridor for detailed analysis.

**Table 1**

Representative open-source AV datasets with applications in safety and crash-risk analysis

| Dataset      | Trajectory coverage <sup>a</sup>         | Safety relevance <sup>b</sup>                         | Duration / Frequency     | HD map | Notes  |
|--------------|--|---|--------------------------|--------|--|
| Argoverse-2  | 250k scenarios; 113 segments; 6 cities   | Near-miss analysis, surrogate safety measures         | 11s per scenario, 10 Hz  | Yes    | Rich lane-level geometry; 10 object classes (Wilson et al. 2023)     |
| nuScenes     | 40k scenes; ~1000 segments; 2 cities     | Multi-agent interactions, trajectory risk indicators  | 20s per scene, 2 Hz      | No     | 23 object classes; widely used urban dataset (Caesar et al. 2020)    |
| Waymo        | 390k scenarios; ~1950 segments; 6 cities | Motion forecasting, crash-prone interaction detection | Up to 20s, 10 Hz         | Yes    | 12.6M trajectories across diverse geometries (Ettinger et al. 2021)  |
| Lyft Level 5 | 170k instances; 1 city                   | Vehicle interactions; trajectory-based safety studies | 25s per instance, 10 Hz  | Yes    | Limited geographic diversity; 10 object classes (Kesten et al. 2019) |
| KITTI        | 15k scenes; 1 city                       | Early surrogate measures, safety benchmarks           | 1–2 min sequences, 10 Hz | No     | Classic full-stack dataset, still widely cited (Geiger et al. 2013)  |
| DAIR-V2X     | 71k frames                               | Infrastructure-based safety monitoring                | –                        | Yes    | First large-scale real-world V2X dataset (Yu et al. 2022)            |
| OPV2V        | 33k samples; CARLA simulation            | Cooperative perception, proactive safety design       | 10 Hz                    | No     | 18k V2X frames, sim environment (Xu et al. 2022)                     |
| DeepAccident | 285k samples; sim dataset                | Rare crash/near-crash events, proactive safety        | 10 Hz                    | Yes    | Includes 57k V2X scenarios (Wang et al. 2024)                        |
| Shift        | 2.5M frames; 4850 segments; 8 cities     | Long-term safety and mobility analysis                | 10 Hz                    | No     | Corridor-scale benchmarking dataset (Sun et al., 2022)               |

<sup>a</sup> **Trajectory coverage:** Number of driving scenarios and geographic spread.

<sup>b</sup> **Safety relevance:** Potential application for crash risk, near-miss, or surrogate safety studies.

#### 4.1.1. Motion forecasting dataset

Each motion forecasting scenario follows a hierarchical structure with three levels: scenario metadata, agent tracks, and frame-level states. Scenarios are 11s duration and are sampled at 10 Hz, producing 110 time steps per vehicle for fine-grained interaction modeling. At the scenario level, metadata includes a unique scenario ID, the recording city, and the focal agent, typically the ego AV. Each scenario then contains multiple agent tracks, where each track corresponds to a road user and specifies the object type (e.g., vehicle, pedestrian, cyclist), scoring category (focal, scored, or unscored), and a time-ordered sequence of states. Frame-level states capture position, velocity, and heading at each timestep, forming the basis for computing 2D-TTC.

To implement the framework, we developed a Python-based batch pipeline using the Argoverse-2 SDK. The pipeline parsed motion forecasting scenarios across all cities and extracted tracks for all agents—not just the focal vehicle—to retain critical multi-agent interactions. For each track, frame-level kinematic attributes were retrieved, including  $(x, y)$  position, heading, velocity components, and timestamps.

Because positions were reported in local, city-specific frames, all coordinates were transformed into a globally referenced WGS84 system. This involved (i) projecting each city’s local origin into its UTM zone (e.g., Zone 17 for Miami, Pittsburgh, and Detroit), and (ii) offsetting local  $(x, y)$  positions and inverse-projecting them to latitude–longitude using `pyproj`. This geospatial normalization provided consistent referencing across cities and ensured compatibility with HD map overlays. Batch scripts automatically traversed scenario folders, performed attribute extraction and coordinate conversion, and exported unified CSV datasets containing both original city-frame and converted lat/lon values. These datasets were then used for spatial filtering, interaction detection, and overlay validation.

The processed files formed the basis for V–V and V–I near-miss detection. For each valid scenario, pairwise distances and relative approach rates were computed for all vehicle pairs, while V–I distances were derived from

buffered polygons of lane edges and curbs in the HD map. Scenarios with no substantive interaction (e.g., straight-lane cruising without lane changes or turns) were excluded, ensuring the dataset emphasized behaviorally informative, high-risk conditions consistent with proactive safety modeling. Non-vehicle agents (e.g., pedestrians, cyclists) were also excluded at this stage, though the pipeline is extensible to incorporate vulnerable road users in future work.

#### 4.1.2. HD map

The Argoverse-2 HD map dataset provides vectorized representations of roadway geometry and drivable space, enabling infrastructure-aware risk estimation. These maps are distributed as JSON files in local city coordinates and contain lane centerlines, left/right boundaries, crosswalk polygons, and drivable area definitions.

Lane-level geometry was extracted using the official Argoverse-2 API. The `get_all_lane_segments()` method returns centerline polylines along with left/right boundaries that define the navigable road space. Additional features, such as crosswalk polygons and drivable area masks, were also retrieved to support validation and visualization, though only lane boundaries and centerlines were directly used in near-miss detection.

Because all coordinates are expressed in city-specific Cartesian frames, global georeferencing was required to align HD maps with trajectory data. For each city, the WGS84 geodetic origin was projected into its respective UTM zone (e.g., Zone 17 for Miami and Pittsburgh, Zone 14 for Austin, Zone 10 for Palo Alto, Zone 18 for Washington, D.C.) using the `pyproj` library. Each local  $(x, y)$  coordinate was then offset by this origin and inverse-projected into latitude–longitude, ensuring spatial consistency across cities. Once transformed, all HD map components: lane boundaries, centerlines, and crosswalks—were indexed using their global coordinates and converted into shapefiles or GeoPandas geometries. This geospatial transformation enabled efficient spatial querying, collision proximity analysis, and visual overlay with satellite imagery and trajectory data. In particular, the lane boundaries were instrumental in detecting V–I near-misses by allowing for the computation of lateral vehicle encroachments beyond the legal driving space. From the processed dataset, a high-density urban corridor in Miami was present to showcase the transformation (see Fig. 3). This illustrates the transformation of AV data into real-world coordinates, its alignment with HD maps and satellite imagery, and the resulting traffic patterns that highlight interaction hotspots across intersections and midblocks.

#### 4.1.3. Trajectory preprocessing and derivation of vehicle dynamics

Before computing 2D-TTC, a series of preprocessing steps was applied to ensure the precision, continuity, and physical plausibility of vehicle motion data from the Argoverse-2 dataset. These steps included the extraction of raw trajectory data, trajectory smoothing and filtering, and the derivation of dynamic variables such as speed, acceleration, and steering angle. First, all multi-agent trajectories were transformed from local city-specific frames to global WGS84 coordinates, enabling consistent alignment with HD map geometries. Raw trajectories were then examined for noise caused by sensor jitter, occlusion, or missed detections—issues more common in human-driven vehicles than in AV tracks. To suppress such noise while preserving curvature and lane-change dynamics, cubic B-spline smoothing was applied to the position coordinates (Eilers and Marx, 1996; Choi et al., 2024). This method effectively removed local fluctuations while retaining key geometric features (see Fig.4). Stationary or irrelevant agents, such as parked vehicles and bicycles, were filtered out to reduce computational load and focus only on interaction-relevant entities.

Dynamic control inputs were then computed. Instantaneous speed  $v_t$  was derived as the Euclidean norm of velocity components:

$$v_t = \sqrt{v_{x,t}^2 + v_{y,t}^2} \quad (33)$$

Residual noise in  $v_t$  was suppressed with a Savitzky–Golay filter (Chen et al., 2004) using a second-order polynomial and a 110-frame window (11s). Longitudinal acceleration ( $a_t$ ) was obtained by first-order numerical differentiation:

$$a_t = \frac{v_{t+1} - v_t}{\Delta t} \quad (34)$$

where  $\Delta t = 0.01$ s reflects the 10 Hz sampling rate. Heading  $\theta_t$  was computed from directional vectors of each track and was unwrapped to maintain continuity across discontinuities at  $\pm\pi$ . The yaw rate  $\dot{\delta}_t$  was derived from the kinematic bicycle model:

$$\dot{\theta}_t = \frac{\theta_{t+1} - \theta_t}{\Delta t} \quad (35)$$

$$\delta_t = \tan^{-1} \left( \frac{L \cdot \dot{\theta}_t}{v_t} \right) \quad (36)$$

The final dataset included per-frame values of speed, acceleration, heading, yaw rate, and steering angle for each track, providing stable and interpretable control inputs. These preprocessed trajectories formed the basis for subsequent near-miss detection using Algorithm 1 and the HBSGRP-UGEV model.

## 4.2. Study area

Under realistic and heterogeneous urban traffic conditions, a representative high-volume corridor was selected along Biscayne Boulevard in Miami, Florida. This arterial extends from Downtown Miami through the Upper East Side toward the northern city limits, serving as a critical connector to major activity centers, including the Miami International Airport region. It is characterized by multimodal interactions, geometric complexity, frequent turning maneuvers, and diverse traffic control features. The corridor was chosen for its rich coverage in the Argoverse-2 motion forecasting dataset, HD map, and its suitability for extracting sufficient samples for extreme near-miss scenarios.

As shown in Fig. 5, the study area was extracted using ArcGIS Pro based on scenario density, HD map fidelity, and heterogeneity of vehicle maneuvers. The extracted network includes a continuous corridor with multiple intersections, midblock segments, and bidirectional traffic operations. For analytical consistency, the corridor was subdivided into nine directional segments (S1–S9) and ten intersections (I1–I10). Segment boundaries were defined midblock to maintain flow continuity, while intersections were delineated to capture near-miss-prone zones such as turning paths, crosswalks, and lane merges. Each subregion was mapped with lane boundaries, crosswalks, and vehicle trajectories to preserve geometric fidelity and directional alignment. Insets in Fig. 5 illustrate the spatial configuration of the segmented units, which serve as the basis for grouped modeling and localized risk estimation.

Table 2 provides a detailed profile of the 28 study subregions, consisting of 10 intersections and 18 directional segments. Intersections generally show fewer scenarios and unique vehicles (e.g., I2 with 47 scenarios and 220 vehicles, I4 with 96 scenarios and 568 vehicles) compared to adjacent midblock segments, reflecting shorter dwell times but higher near-miss intensity. In contrast, segments accumulate a significantly higher number of scenarios and vehicles due to sustained travel. For example, S7 (NE 19–17 St) records 308 northbound and 332 southbound scenarios involving more than 4000 vehicles, while S8 (NE 17–15 St) captures nearly 4400 vehicles in 608 scenarios.

Lane configurations vary between 2 and 3 lanes per direction, with average widths ranging from 3.1 m (S7) to 3.6 m (S6), indicating subtle but important differences in cross-sectional design. Driveway and minor intersection density also differ across the corridor: segments such as S3 and S4 contain four access points, while others like S5 and S6 have few or none, creating heterogeneous exposure to side-entry near-misses. The median type alternates between raised (e.g., S1–S2) and flush-paved (e.g., S3–S9), influencing turning maneuvers and mid-block encroachments. Overall, the table highlights that intersections serve as near-miss-prone nodes with concentrated but lower-volume interactions, whereas segments provide richer samples of continuous traffic flow, characterized by greater geometric variability.

Building on the spatial segmentation and detailed subregion profiles outlined above, the next step involves quantifying dynamic safety conditions using the proposed 2D-TTC framework (Algorithm 1). For each block, extreme near-miss events were identified by forward simulating vehicle trajectories under the geometric and traffic conditions described in Table 2. Both V–V and V–I interactions were modeled to reflect the heterogeneous near-miss environments of intersections and segments. Trajectories were projected over a 3s horizon, and spatial overlaps with surrounding traffic or roadway boundaries were detected as potential near-miss events. Representative outcomes from this process are shown in Fig. 6, illustrating the spatial dynamics of predicted V–V and V–I near-misses within the Miami study corridor. These event visualizations provide the empirical basis for block-level 2D-TTC extraction across the 10 intersections (I1–I10), enabling localized evaluation of crash-prone conditions.

Descriptive statistics of intersection-level V–V and V–I near-misses are summarized in Table 3. The continuous indicators include 2D-TTC, relative speed, acceleration, distance, jerk, and angular deviations (heading and steering), along with vehicle dimensions and exposure (volume). On average, 2D-TTC values for both near-miss types range between 1.3 and 1.6 s, with extreme cases falling below 0.1 s, reflecting highly critical near-miss conditions. V–I

**Table 2**  
Profile of study locations along Biscayne Boulevard

| ID                  | Location      | Direction | Scenarios | Unique vehicles | Lane no | Lane width (m) | Driveway/Minor intersection | Median type |
|---------------------|---------------|-----------|-----------|-----------------|---------|----------------|-----------------------------|-------------|
| <i>Segment</i>      |               |           |           |                 |         |                |                             |             |
| S1                  | (NE 36–33 St) | NB / SB   | 131 / 111 | 1706 / 813      | 3 / 3   | 3.5            | 3                           | Raised      |
| S2                  | (NE 33–29 St) | NB / SB   | 151 / 155 | 1532 / 1148     | 3 / 3   | 3.64           | 3                           | Raised      |
| S3                  | (NE 29–26 St) | NB / SB   | 191 / 186 | 1721 / 1295     | 3 / 3   | 3.36           | 4                           | Flush paved |
| S4                  | (NE 26–22 St) | NB / SB   | 176 / 199 | 1542 / 1581     | 3 / 3   | 3.51           | 4                           | Flush paved |
| S5                  | (NE 22–21 St) | NB / SB   | 127 / 123 | 705 / 643       | 3 / 2   | 3.3            | No                          | Flush paved |
| S6                  | (NE 21–19 St) | NB / SB   | 235 / 245 | 1588 / 1861     | 3 / 3   | 3.62           | 1                           | Flush paved |
| S7                  | (NE 19–17 St) | NB / SB   | 308 / 332 | 1704 / 2410     | 2 / 2   | 3.12           | 1                           | Flush paved |
| S8                  | (NE 17–15 St) | NB / SB   | 294 / 314 | 1955 / 2406     | 3 / 3   | 3.57           | 2                           | Flush paved |
| S9                  | (NE 15–13 St) | NB / SB   | 232 / 216 | 1565 / 1217     | 3 / 2   | 3.43           | 1                           | Flush paved |
| <i>Intersection</i> |               |           |           |                 |         |                |                             |             |
| I1                  | NE 36 St      | –         | 97        | 743             | –       | –              | –                           | –           |
| I2                  | NE 33 St      | –         | 47        | 220             | –       | –              | –                           | –           |
| I3                  | NE 29 St      | –         | 132       | 699             | –       | –              | –                           | –           |
| I4                  | NE 26 St      | –         | 96        | 568             | –       | –              | –                           | –           |
| I5                  | NE 22 St      | –         | 106       | 640             | –       | –              | –                           | –           |
| I6                  | NE 21 St      | –         | 134       | 647             | –       | –              | –                           | –           |
| I7                  | NE 19 St      | –         | 214       | 1332            | –       | –              | –                           | –           |
| I8                  | NE 17 St      | –         | 205       | 1328            | –       | –              | –                           | –           |
| I9                  | NE 15 St      | –         | 252       | 1332            | –       | –              | –                           | –           |
| I10                 | NE 13 St      | –         | 232       | 1139            | –       | –              | –                           | –           |

**Table 3**  
Summary statistics for V–V and V–I near-misses at Intersection

| Metric   | V–V    |         |        |       | V–I    |         |        |        |
|--|--------|---------|--------|-------|--------|---------|--------|--------|
|  | Avg    | Min     | Max    | Std   | Avg    | Min     | Max    | Std    |
| <i>Continuous variables</i>                                    |        |         |        |       |        |         |        |        |
| TTC  | 1.617  | 0.11    | 2.99   | 0.863 | 1.304  | 0.10    | 2.99   | 0.889  |
| Relative speed   | 5.257  | 0.00    | 23.724 | 4.446 | 8.753  | 0.00    | 22.276 | 4.035  |
| Relative acc/dec   | -0.535 | -13.706 | 10.343 | 2.227 | 0.161  | -5.925  | 13.199 | 0.702  |
| Relative distance  | 11.673 | 2.419   | 46.857 | 6.844 | 1.520  | 0.60    | 3.80   | 1.110  |
| Jerk   | -5.550 | -13.609 | 9.315  | 2.652 | -7.900 | -10.800 | 2.800  | 14.700 |
| Heading difference   | 1.077  | 0.00    | 6.251  | 1.410 | -0.045 | -3.138  | 3.141  | 1.647  |
| Steering difference  | 0.409  | 0.00    | 3.142  | 0.666 | -0.006 | -1.571  | 1.571  | 0.130  |
| Volume   | 13.462 | 2.00    | 31.00  | 5.969 | 10.461 | 1.00    | 31.00  | 5.392  |
| Vehicle length   | 4.78   | 3.18    | 6.92   | 0.49  | 5.1    | 3.95    | 12.65  | 1.30   |
| Vehicle width  | 2.22   | 1.76    | 3.16   | 0.30  | 2.04   | 1.36    | 3.08   | 0.23   |
| <i>Categorical variable: Near-miss location (Proportion %)</i> |        |         |        |       |        |         |        |        |
| Through  | 72.29  |         |        | 0.00  |        |         |        |        |
| Left Turn  | 25.99  |         |        | 46.08 |        |         |        |        |
| Right Turn   | 8.90   |         |        | 53.92 |        |         |        |        |

near-misses are associated with higher relative speeds and tighter distance gaps, indicating more abrupt encroachment against roadway boundaries. Conversely, V–V near-misses exhibit larger heading and steering deviations, along with higher jerk variability, suggesting unstable maneuvers such as sudden turns or evasive swerves. The categorical distribution of near-misses further illustrates key behavioral differences. Nearly three-quarters (72%) of V–V events occurred during through movements, with fewer during left (26%) or right (9%) turns. In contrast, V–I near-misses were almost entirely turning-related, with 46% occurring in left turns and 54% in right turns, and none during through movements. This pattern highlights that infrastructure-related near-misses typically occur during lateral maneuvers at intersections, where vehicles cross lane boundaries or encroach on curbs and medians.

Beyond intersections, the analysis was extended to directional roadway segments (S1–S9) using the same 2D-TTC framework (See Fig. 7). Table 4 summarizes descriptive statistics of both V–V and V–I near misses at the segment level.

**Table 4**  
Summary statistics for V–V and V–I near-misses at segments

| Metric                               | V–V        |         |         |        | V–I    |         |        |       |
|--------------------------------------|------------|---------|---------|--------|--------|---------|--------|-------|
|                                      | Avg        | Min     | Max     | Std    | Avg    | Min     | Max    | Std   |
| Continuous variables                 |            |         |         |        |        |         |        |       |
| TTC                                  | 1.829      | 0.11    | 2.99    | 0.805  | 1.272  | 0.10    | 2.99   | 0.912 |
| Relative speed                       | 4.513      | 0.00    | 33.909  | 4.278  | 10.262 | 0.000   | 28.067 | 4.212 |
| Relative acc/dec                     | -0.871     | -23.014 | 18.336  | 3.139  | 0.164  | -14.067 | 23.343 | 1.400 |
| Relative distance                    | 15.361     | 1.931   | 141.548 | 12.773 | 1.720  | 0.32    | 6.56   | 1.02  |
| Jerk                                 | -7.121     | -17.502 | 8.423   | 1.552  | -5.70  | -12.72  | 3.556  | 4.77  |
| Heading difference                   | 0.368      | 0.000   | 6.256   | 0.990  | -0.032 | -3.102  | 3.138  | 1.586 |
| Steering difference                  | 0.577      | 0.000   | 3.142   | 0.756  | -0.001 | -1.571  | 1.571  | 0.167 |
| Volume                               | 16.801     | 1.000   | 65.000  | 11.009 | 12.816 | 1.000   | 65.000 | 7.906 |
| Vehicle Length                       | 4.74       | 3.0     | 7.85    | 1.11   | 4.79   | 2.95    | 8.65   | 0.87  |
| Vehicle width                        | 2.12       | 1.36    | 3.08    | 0.23   | 2.22   | 1.76    | 4      | 0.18  |
| Lane number                          | 2.73       | 2       | 4       | 0.578  | 2.51   | 2.0     | 4.0    | 0.52  |
| Lane width                           | 3.28       | 2.99    | 3.96    | 0.14   | 3.27   | 2.99    | 3.96   | 0.141 |
| Driveway intensity                   | 0.009      | 0.000   | 0.015   | 0.005  | 0.009  | 0.000   | 0.015  | 0.005 |
| Categorical variable: (Proportion %) |            |         |         |        |        |         |        |       |
| Collision location                   | Through    |         | 58.55   |        |        | 0.00    |        |       |
|                                      | Left Turn  |         | 9.52    |        |        | 46.08   |        |       |
|                                      | Right Turn |         | 31.93   |        |        | 53.92   |        |       |
| Median type                          | Divided    |         | 23.60   |        |        | 13.98   |        |       |
|                                      | Undivided  |         | 76.4    |        |        | 86.02   |        |       |

For V–V near-misses, average TTC values were longer (1.83 s) than those observed at intersections, suggesting greater temporal headway between vehicles in segment settings. However, the extreme minima (0.11 s) and high maximum relative speeds (up to 33.9 m/s) highlight the presence of aggressive overtaking and high-speed convergence. Relative distances also exhibited a much broader range (up to 141.5 m), indicating that near-misses often arise in more dispersed longitudinal interactions rather than tightly constrained intersection maneuvers.

For V–I near-misses, the mean TTC was shorter (1.27s), with relative speeds peaking at 28.1 m/s, underscoring the abrupt nature of vehicle–boundary encounters. Compared with intersections, segment-based V–I near-misses involved longer approach distances but also showed greater instability in jerk and heading, reflecting frequent lateral drifts toward lane edges or curbs. These events often occurred near driveways and minor access points, where vehicles deviated from their intended path, creating encroachment risks. The categorical breakdown reinforces these patterns. For V–V events, nearly 59% of near-misses were associated with through movements, while about 32% and 10% were linked to right and left turns, respectively. In contrast, V–I near-misses were dominated by turning maneuvers, with more than half (53.9%) linked to right turns and 46% to left turns, and no near-misses detected during through movements. This distribution highlights the heightened role of lateral maneuvers in producing infrastructure-related risks. Furthermore, median type also influenced outcomes: 76% of V–V near-misses and 86% of V–I near-misses occurred along undivided sections, underscoring the vulnerability of open medians and flush-paved designs in segment environments.

Taken together, these segment-level findings reveal that while intersections are hotspots for tightly constrained V–V near-misses, segments carry distinctive risks tied to high-speed encounters and infrastructure encroachments. The observed distributions underscore the importance of treating intersections and segments as functionally distinct safety domains when modeling near-miss dynamics and designing targeted countermeasures.

After identifying and compiling the BM near-miss events for each observation unit (segments and intersections), the frequencies of extreme V–V and V–I events were systematically aggregated and visualized in Fig. 8. This plot illustrates the spatial distribution of extreme near-miss frequencies across 28 locations, comprising 10 intersections and 18 segments, organized into intersection zones, primary-direction segments, and opposite-direction segments. This spatial

aggregation confirms the integrity of the BM dataset and provides the foundation for modeling. The study extends prior approaches by incorporating both V–V and V–I near misses into the HBSGRP–UGEV framework, explicitly integrating roadway geometry and infrastructure features alongside vehicle dynamics. Prior research has emphasized the role of vehicle kinematics in crash risk (Desai et al., 2021; Jun et al., 2007; Tak et al., 2015); here, additional geometric covariates, such as lane configuration and boundary proximity, are introduced. For example, high steering angles, often indicating abrupt lateral maneuvers, were included as predictors, given their link to boundary incursions and sudden evasive actions that may elevate near-miss risk (Gilbert et al., 2021). Fig. 8 highlights several notable spatial patterns. Opposite-direction segments (S82, S72, S62) exhibited the highest V–I frequencies, suggesting greater lateral variability and exposure to curb or median near-misses. Primary-direction segments (S11, S21, S81) showed elevated V–V near-miss frequencies, consistent with midblock environments dominated by longitudinal interactions such as close-following, lane changes, or overtaking. Among intersections, I7, I8, and I9 emerged as critical hotspots, with elevated frequencies of both near-miss types. This dual concentration reflects the operational complexity of intersections, where near-missing maneuvers, pedestrian flows, and signal control interact to amplify crash potential.

The distribution and magnitude of near-miss counts across all locations validate the effectiveness of the BM approach in capturing rare but safety-critical events. Specifically, nearly all study sites meet or exceed the recommended minimum threshold of 30 BM events for reliable GEV-based inference (Zheng et al., 2014), with the exception of intersection I2. This ensures that the dataset is statistically robust for subsequent HBSGRP–UGEV analysis. The spatial heterogeneity revealed in Fig. 8 further underscores the need to incorporate direction-specific geometric and behavioral covariates within the modeling framework. These results provide compelling justification for developing localized, high-resolution safety models that integrate both roadway configuration and observed vehicle dynamics, thereby enabling precise and context-sensitive real-time risk assessments in complex urban environments.

## 5. Modeling estimation result

This study develops a series of Bayesian hierarchical UGEV models to estimate corridor-wide COR from extreme 2D-TTC near-miss events observed along Biscayne Boulevard in Miami. Extreme near-misses are identified using the BM approach, wherein the minimum 2D-TTC within each temporal block is treated as the most critical interaction. The theoretical basis and implementation of this sampling methodology are detailed in prior work (2025b). Each V–V and V–I interaction is treated as an independent block. Since extreme events are relatively sparse at individual sites, direct location-specific estimation often yields unstable posteriors with wide uncertainty intervals. To address this issue, a corridor-wide grouping strategy was adopted, pooling samples across functionally similar sites (intersections, segments) while preserving local heterogeneity.

The HBSGRP–UGEV model is the primary analytical framework, with a simpler fixed-effect hierarchical model (HBSFP) also estimated for comparison. For each near-miss type (V–V and V–I), two models were therefore developed: (1) HBSFP and (2) HBSGRP. The grouped random parameter formulation in HBSGRP allows selected coefficients to vary across spatial clusters, thereby capturing latent heterogeneity associated with interaction dynamics and roadway characteristics. Model performance was evaluated using the DIC (Spiegelhalter et al., 2002; El-Basyouny and Sayed, 2012b,a), with lower values indicating superior predictive fit (Zheng et al., 2019).

Estimation was conducted using MultiBUGS, a parallelized extension of OpenBUGS tailored for high-dimensional Bayesian inference. Its support for block updating and parallel execution makes it well-suited to modeling spatial dependence, random effects, and extreme value behavior within complex data structures. Parameters were estimated by Markov Chain Monte Carlo (MCMC) simulation; two parallel MCMC chains of 50000 iterations were run, with the first 20000 discarded as burn-in and the remaining 30000 retained for posterior inference. Convergence was assessed both visually (trace plots) and quantitatively (Brooks–Gelman–Rubin diagnostic), with all monitored parameters achieving BGR values below 1.1, confirming reliable convergence (Gelman and Rubin, 1992; Brooks and Gelman, 1998; El-Basyouny and Sayed, 2009). This procedure yielded robust posterior summaries of means, standard deviations, and 95% credible intervals, even under correlation structures induced by spatial clustering and random effects.

The modeling framework incorporated a comprehensive set of covariates into the location ( $\mu$ ) and scale ( $\sigma$ ) parameters of the nonstationary UGEV distribution to capture contextual and behavioral variability in COR. For both V–V and V–I interactions, dynamic covariates included relative (speed, distance, acceleration, deceleration, headway, steering angle), jerk, and traffic volume, thereby capturing multiple dimensions of vehicle dynamics. Geometric and infrastructure related covariates were also included: lane number, lane width, driveway intensity, median type, and lane position of vehicle.

All covariates were specified in both the  $\mu$  and  $\sigma$  components, enabling the models to capture variation in both the central tendency and dispersion of extreme 2D-TTC. In contrast, the shape parameter ( $\xi$ ) was held constant across all locations. This decision reflects a tradeoff between flexibility and stability: although  $\xi$  governs tail heaviness in the UGEV distribution, it is notoriously difficult to estimate from sparse BM samples. Allowing  $\xi$  to vary with covariates often induces instability and overfitting (Coles et al., 2001; Cooley et al., 2006), whereas fixing it improves convergence and yields more interpretable posterior distributions.

## 5.1. Posterior results and model performance

Tables 5 through 8 report the posterior summaries for both HBSFP and HBSGRP models, estimated separately for V–V and V–I near-misses at intersections and segments. Across all cases, the HBSGRP structure consistently outperformed the HBSFP baseline model, confirming its capacity to capture unobserved heterogeneity and location-level variability. The DIC values for the HBSGRP models were 508.9 (V–V) and 3179.6 (V–I) at intersections, and 4189.0 (V–V) and 6550.0 (V–I) at segments. These correspond to relative reductions of 3.41% and 0.54% at intersections, and 7.49% and 3.11% at segments, compared with their HBSFP counterparts. Such improvements exceed the widely accepted threshold of five DIC units, indicating substantively better model fit (El-Basyouny and Sayed, 2012b,a). To further evaluate robustness, WAIC and LOOIC were also computed, both of which produced rankings consistent with DIC, thereby reinforcing the superior performance of the HBSGRP. By allowing selected coefficients to vary across spatial groups, the HBSGRP models capture latent heterogeneity in both the central tendency and dispersion, a capability absent in fixed-effect structures. Collectively, these results demonstrate that grouped random parameter models provide a more flexible and accurate framework for modeling COR dynamics in complex urban traffic environments.

### 5.1.1. Intersection-level

The intersection-level HBSGRP–UGEV model was designed to capture the heterogeneity of extreme 2D-TTC distributions from V–V interactions at signalized intersections. In the modeling stage, all covariates were considered as random effects; however, roadway characteristics and few vehicle dynamics were exhibited negligible variation across sites and did not improve posterior fit. To maintain parsimony and interpretability, random effects were restricted to the intercept and two dynamic covariates (relative speed and distance), while other covariates were retained as fixed effects, following recommendations from (Anis et al., 2025a). This choice reflects theoretical expectations: vehicle dynamics are highly variable across intersections depending on signal phasing, approach alignment, and driver behavior, whereas roadway structure tends to exert a more stable influence. The resulting specification captures both site-specific dynamics and broader geometric constraints, group-specific random effects illustrated in Fig. 9 with posterior summaries reported in Table 5.

Consistent reductions in DIC, WAIC, and LOOIC confirm the superior fit of the HBSGRP model, highlighting the added value of allowing speed and spacing effects to vary across intersections. The direction and magnitude of these coefficients provide insights into the mechanisms underlying COR. Relative speed and distance emerge as the dominant dynamics, influencing both the location ( $\mu$ ) and scale ( $\sigma$ ) parameters. For  $\mu$ , relative speed has a positive effect, indicating that larger speed differentials between vehicles sharply reduce 2D-TTC and intensify near-miss severity. In contrast, relative distance shows a negative effect, meaning shorter headways systematically elevate severity by limiting available buffer space for evasive action. For  $\sigma$ , both covariates carry negative signs, implying that high speeds and short distances compress variability, yielding consistently critical outcomes with little room for driver recovery through braking or swerving. Taken together, these results confirm that speed amplifies severity while short headways exacerbate risk and reduce variability, producing deterministic near-miss outcomes under constrained conditions. Fig. 9 illustrates the spatial heterogeneity across intersections. While most locations show consistent trends, the I2 site exhibits unusually wide credible intervals for the  $\mu$  effects and intervals exceeding zero for the  $\sigma$  across the intercept, relative speed, and relative distance. This instability is attributable to I2's small BM sample size, which weakens posterior precision and increases uncertainty in group-level effects. Despite localized uncertainty, the dominant intersection-level trend persists, with relative speed and distance exerting stable and significant effects on near-miss outcomes.

Beyond random effects, several covariates were modeled as fixed parameters due to their stable contributions across intersections. These effects can be interpreted in terms of driver behavior. These factors highlight the roles of longitudinal dynamics, lateral control, maneuver type, and exposure in shaping near-miss outcomes. Table 5 shows that relative acceleration has a significant negative effect on both the location and scale parameters, suggesting smoother and less variable near misses when vehicles accelerate through green phases or clear intersections without abrupt

**Table 5**  
Posterior estimates for V-V near misses at intersections

| Model Parameters  | Hyperparameter | Covariate                       | HBSFP  |                 |                               | HBSGRP |                 |                               |
|---|----------------|---------------------------------|--------|-----------------|-------------------------------|--------|-----------------|-------------------------------|
|   |                |                                 | Mean   | SD <sup>a</sup> | 95% CRI <sup>b</sup>          | Mean   | SD <sup>a</sup> | 95% CRI <sup>b</sup>          |
| <i>Location Parameter (<math>\mu_{k,l}</math>)</i>      |                |                                 |        |                 |                               |        |                 |                               |
| $\beta_{\mu,0}$   | Fixed          | Intercept                       | -1.870 | 0.039           | [-1.917, -1.811] <sup>†</sup> | -      | -               | -                             |
| $\beta_{\mu,0,k}$                                       | Random         | Intercept                       | -      | -               | -                             | -1.893 | 0.186           | [-2.309, -1.572] <sup>†</sup> |
| $\gamma_{\mu,1,k}$                                      | Random         | Relative speed                  | -      | -               | -                             | 0.745  | 0.181           | [0.393, 1.134] <sup>†</sup>   |
| $\gamma_{\mu,2,k}$                                      | Random         | Relative distance               | -      | -               | -                             | -0.491 | 0.157           | [-0.819, -0.280] <sup>†</sup> |
| $\beta_{\mu,1}$   | Fixed          | Relative speed                  | 0.639  | 0.050           | [0.246, 0.739] <sup>†</sup>   | -      | -               | -                             |
| $\beta_{\mu,2}$   | Fixed          | Relative acceleration           | 1.064  | 0.074           | [0.126, 2.018] <sup>†</sup>   | -0.155 | 0.032           | [-0.221, -0.093] <sup>†</sup> |
| $\beta_{\mu,3}$   | Fixed          | Relative deceleration           | -0.013 | 0.037           | [-0.088, 0.059] <sup>†</sup>  | 0.140  | 0.063           | [0.004, 0.238] <sup>†</sup>   |
| $\beta_{\mu,4}$   | Fixed          | Relative distance               | -0.442 | 0.036           | [-0.505, -0.418] <sup>†</sup> | -      | -               | -                             |
| $\beta_{\mu,5}$   | Fixed          | Jerk                            | -0.012 | 0.006           | [-0.021, -0.002] <sup>†</sup> | -0.027 | 0.015           | [-0.046, -0.006] <sup>†</sup> |
| $\beta_{\mu,6}$   | Fixed          | Heading difference              | 0.024  | 0.026           | [-0.029, 0.072] <sup>†</sup>  | 0.028  | 0.039           | [-0.052, 0.097] <sup>†</sup>  |
| $\beta_{\mu,7}$   | Fixed          | Steering difference             | -0.004 | 0.049           | [-0.096, 0.092] <sup>†</sup>  | 0.059  | 0.026           | [0.003, 0.107] <sup>†</sup>   |
| $\beta_{\mu,8}$   | Fixed          | Volume                          | -0.003 | 0.005           | [-0.012, 0.006] <sup>†</sup>  | -0.018 | 0.035           | [-0.085, 0.051] <sup>†</sup>  |
| $\beta_{\mu,9}$   | Fixed          | Turn movement (Left =1, else=0) | 0.086  | 0.026           | [-0.102, 0.242] <sup>†</sup>  | 0.073  | 0.011           | [0.042, 0.205] <sup>†</sup>   |
| <i>Scale Parameter (<math>\log \sigma_{k,l}</math>)</i> |                |                                 |        |                 |                               |        |                 |                               |
| $\beta_{\sigma,0}$                                      | Fixed          | Intercept                       | -0.571 | 0.058           | [-0.680, -0.455] <sup>†</sup> | -      | -               | -                             |
| $\beta_{\sigma,0,k}$                                    | Random         | Intercept                       | -      | -               | -                             | -0.599 | 0.311           | [-1.240, -0.056] <sup>†</sup> |
| $\gamma_{\sigma,1,k}$                                   | Random         | Relative speed                  | -      | -               | -                             | -0.265 | 0.254           | [-0.810, -0.043] <sup>†</sup> |
| $\gamma_{\sigma,2,k}$                                   | Random         | Relative distance               | -      | -               | -                             | -0.653 | 0.297           | [-1.121, -0.033] <sup>†</sup> |
| $\beta_{\sigma,1}$                                      | Fixed          | Relative speed                  | 0.012  | 0.084           | [-0.139, 0.183] <sup>†</sup>  | -      | -               | -                             |
| $\beta_{\sigma,2}$                                      | Fixed          | Relative acceleration           | -1.686 | 0.865           | [-3.066, -0.627] <sup>†</sup> | -0.226 | 0.066           | [-0.360, -0.108] <sup>†</sup> |
| $\beta_{\sigma,3}$                                      | Fixed          | Relative deceleration           | -0.218 | 0.051           | [-0.321, -0.120] <sup>†</sup> | -0.253 | 0.053           | [-0.356, -0.151] <sup>†</sup> |
| $\beta_{\sigma,4}$                                      | Fixed          | Relative distance               | -0.062 | 0.008           | [-0.078, -0.046] <sup>†</sup> | -      | -               | -                             |
| $\beta_{\sigma,5}$                                      | Fixed          | Jerk                            | 0.019  | 0.009           | [0.005, 0.030] <sup>†</sup>   | 0.012  | 0.003           | [0.007, 0.018] <sup>†</sup>   |
| $\beta_{\sigma,6}$                                      | Fixed          | Heading difference              | -0.063 | 0.071           | [-0.212, 0.060] <sup>†</sup>  | -0.055 | 0.014           | [-0.133, -0.026] <sup>†</sup> |
| $\beta_{\sigma,7}$                                      | Fixed          | Steering difference             | 0.063  | 0.065           | [-0.061, 0.191] <sup>†</sup>  | -0.053 | 0.040           | [-0.117, -0.011] <sup>†</sup> |
| $\beta_{\sigma,8}$                                      | Fixed          | Volume                          | -0.001 | 0.007           | [-0.015, 0.013] <sup>†</sup>  | -0.004 | 0.044           | [-0.090, 0.084] <sup>†</sup>  |
| $\beta_{\sigma,9}$                                      | Fixed          | Turn movement(Left =1, else=0)  | 0.042  | 0.120           | [-0.183, 0.285] <sup>†</sup>  | 0.217  | 0.123           | [0.025, 0.471] <sup>†</sup>   |
| <i>Shape Parameter (<math>\xi_{k,l}</math>)</i>         |                |                                 |        |                 |                               |        |                 |                               |
| $\beta_{\xi,0}$   | Fixed          | Intercept                       | -0.305 | 0.051           | [-0.413, -0.208] <sup>†</sup> | -      | -               | -                             |
| $\beta_{\xi,0,k}$                                       | Random         | Intercept                       | -      | -               | -                             | -0.684 | 0.253           | [-1.309, -0.314] <sup>†</sup> |
| <i>Model Fit</i>  |                |                                 |        |                 |                               |        |                 |                               |
| DIC   |                |                                 | 526.9  |                 |                               | 508.9  |                 |                               |
| WAIC  |                |                                 | 539.4  |                 |                               | 521.5  |                 |                               |
| LOOIC   |                |                                 | 540.1  |                 |                               | 522.3  |                 |                               |

HBSFP Hierarchical Bayesian Spatial Fixed Parameter  
HBSGRP Hierarchical Bayesian Spatial Grouped Random Parameter

<sup>a</sup> Standard deviation

<sup>b</sup> 95% Bayesian credible interval

- Covariate not included in the model

<sup>†</sup> Indicates statistical significance at the 95% level (interval excludes 0)

interaction. By contrast, relative deceleration increases severity ( $\mu$ ) but reduces variability ( $\sigma$ ), capturing emergency braking events. These situations sharply intensify near misses but also produce uniform outcomes, since drivers in crisis have limited response options. Jerk, representing the rate of change in acceleration, shows the opposite pattern: a negative effect on  $\mu$  but a positive effect on  $\sigma$ . This suggests that rapid throttle-brake oscillations, often signs of hesitation or overcorrection, slightly lower average severity but introduce greater unpredictability, underscoring the instability of abrupt corrective maneuvers.

Lateral vehicle dynamics also play an important role in near-miss risk estimation. Steering difference is a significant factor in the HBSGRP model, showing a positive association with  $\mu$  and a negative association with  $\sigma$ . This indicates that abrupt steering maneuvers intensify near-miss severity but produce more consistent outcomes within constrained intersection geometries. Heading difference shows a similar pattern, with a positive effect on  $\mu$  and a negative effect on  $\sigma$ . This suggests that even small misalignments in vehicle trajectory elevate severity while reducing variability, reflecting the rigid geometric constraints of signalized approaches.

The categorical indicator for left-turn movements is significant, with positive effects on both  $\mu$  and  $\sigma$ . This finding is consistent with the well-documented complexity of left-turn phases, which involve interactions with opposing through traffic and diverse driver decision strategies. Left turns therefore not only elevate near-miss severity but also increase variability, reflecting differences in intersection design and driver behavior under turning conditions. By contrast, traffic volume is statistically insignificant for both parameters but was retained in the model to represent exposure. Its lack of effect suggests that short-duration extreme 2D-TTC events are driven more by instantaneous vehicle interactions than by aggregate demand.

Finally, the estimated shape parameter ( $\xi$ ) is negative and significant across all intersections (Fig. 9g), indicating a bounded upper tail of the UGEV distribution. This supports the Weibull domain as the appropriate tail form for modeling extreme near-misses in signalized urban settings. Importantly, group-level variability in  $\xi$  suggests that intersection design and control strategies influence not only the frequency but also the extremal nature of near-miss outcomes.

The HBSGRP model for V-I near misses specified the intercept as a random parameter in both the location and scale components, capturing baseline heterogeneity in severity and variability across intersections. Relative speed (in  $\mu$ ) and relative distance (in  $\sigma$ ) were also modeled as random effects (Fig. 10), although their 95% credible intervals overlapped zero. They were nevertheless retained on theoretical grounds, as their inclusion improved overall model fit. This specification reflects behavioral intuition: heterogeneity in speed effects is more pronounced in severity (location), whereas heterogeneity in clearance effects is more evident in variability (scale). All other covariates were treated as fixed effects, reflecting their comparatively stable behavioral and geometric influences. Fit statistics (Table 6) show modest but consistent improvements in DIC, WAIC, and LOOIC relative to the HBSFP specification, suggesting that the grouped random parameter structure adds explanatory nuance but produces smaller performance gains than in the V-V case.

In the location parameter, several interpretable effects emerge. Relative distance is strongly negative and significant, confirming that reduced clearance to the roadway edge sharply lowers 2D-TTC and elevates severity. Relative deceleration also enters with a significant negative sign, contrasting with its positive effect in V-V near misses. This suggests that braking near infrastructure often reflects proactive yielding or evasive maneuvers, which mitigate severity rather than intensify it. Heading and steering differences are positive and significant, indicating that lateral deviations (e.g., turning toward or away from curbs) increase near-miss severity. Left-turn movement, by contrast, shows a significant negative association, suggesting that left-turn trajectories provide greater clearance to boundaries and reduce severity compared with right turns. This pattern may reflect geometric characteristics such as wider turning radii or reduced overlap with curbs and crosswalks during left-turn phasing. Finally, relative speed—although modeled as a random effect—does not reach significance in the pooled analysis, reinforcing that V-I severity is less sensitive to speed differentials than V-V encounters.

The scale parameter results provide additional insight into variability. The negative random intercept indicates baseline differences across intersections, with some sites producing more predictable outcomes than others. Relative speed shows a positive and significant association with  $\sigma$ , implying that faster approaches to infrastructure increase variability in severity—in contrast to the V-V case, where speed compressed dispersion. This divergence reflects the diverse ways drivers respond to boundary proximity: some brake aggressively, while others maintain speed or adjust trajectory. Relative acceleration is also positive and significant, reinforcing that heterogeneous acceleration behavior near boundaries broadens outcome variability. By contrast, relative deceleration has a significant negative effect, indicating that decisive braking compresses the distribution into consistently critical outcomes. Jerk is similarly positive, confirming that abrupt throttle-brake oscillations amplify variability. Lateral dynamics play the opposite role: heading and steering differences both reduce variability, suggesting that once a lateral maneuver is committed, outcomes become more predictable within intersection geometry. Finally, left-turn movement increases variability despite lowering mean severity, consistent with heterogeneous layouts and driver strategies in left-turn contexts.

The shape parameter remains negative and significant across intersections, supporting the Weibull domain for V-I near misses and confirming that these events have a bounded upper tail. This indicates a physical and behavioral ceiling on severity, constrained by roadway geometry and driver response capacity. Spatial variation in  $\xi$  further underscores the influence of intersection design and infrastructure placement on the extremal properties of near-miss distributions. Taken together, the intersection-level results suggest that V-I near misses are shaped more by clearance, braking, and lateral maneuvers than by speed differentials. In contrast, V-V near misses are dominated by high speeds, which produce deterministic severity, whereas V-I outcomes exhibit greater variability driven by the interplay of infrastructure geometry, driver avoidance strategies, and intersection control.

**Table 6**  
Posterior estimates for V-I near misses at intersections

| Model Parameters  | Hyperparameter | Covariate                       | HBSFP   |                 |                                | HBSGRP |                 |                               |
|---|----------------|---------------------------------|---------|-----------------|--------------------------------|--------|-----------------|-------------------------------|
|   |                |                                 | Mean    | SD <sup>a</sup> | 95% CRI <sup>b</sup>           | Mean   | SD <sup>a</sup> | 95% CRI <sup>b</sup>          |
| <i>Location Parameter (<math>\mu_{k,i}</math>)</i>      |                |                                 |         |                 |                                |        |                 |                               |
| $\beta_{\mu,0}$   | Fixed          | Intercept                       | -1.392  | 0.039           | [-1.461, -1.299] <sup>†</sup>  | -      | -               | -                             |
| $\beta_{\mu,0,k}$                                       | Random         | Intercept                       | -       | -               | -                              | -1.401 | 0.092           | [-1.598, -1.236] <sup>†</sup> |
| $\gamma_{\mu,1,k}$                                      | Random         | Relative speed                  | -       | -               | -                              | 0.025  | 0.020           | [-0.012, 0.065]               |
| $\beta_{\mu,1}$   | Fixed          | Relative speed                  | -0.012  | 0.022           | [-0.054, 0.031]                | -      | -               | -                             |
| $\beta_{\mu,2}$   | Fixed          | Relative acceleration           | -0.020  | 0.023           | [-0.067, 0.022]                | -0.020 | 0.024           | [-0.068, 0.029]               |
| $\beta_{\mu,3}$   | Fixed          | Relative deceleration           | -0.066  | 0.013           | [-0.075, -0.055] <sup>†</sup>  | -0.026 | 0.011           | [-0.071, -0.009] <sup>†</sup> |
| $\beta_{\mu,4}$   | Fixed          | Relative distance               | -0.357  | 0.035           | [-0.427, -0.290] <sup>†</sup>  | -0.359 | 0.026           | [-0.405, -0.306] <sup>†</sup> |
| $\beta_{\mu,5}$   | Fixed          | Jerk                            | 0.270   | 0.355           | [-0.457, 0.556]                | -0.021 | 0.005           | [-0.026, 0.01]                |
| $\beta_{\mu,6}$   | Fixed          | Heading difference              | 0.040   | 0.022           | [0.005, 0.084] <sup>†</sup>    | 0.062  | 0.026           | [0.010, 0.127] <sup>†</sup>   |
| $\beta_{\mu,7}$   | Fixed          | Steering difference             | 0.009   | 0.018           | [-0.027, 0.045]                | 0.038  | 0.022           | [0.014, 0.074] <sup>†</sup>   |
| $\beta_{\mu,8}$   | Fixed          | Volume                          | -0.017  | 0.021           | [-0.061, 0.023]                | -0.023 | 0.023           | [-0.069, 0.027]               |
| $\beta_{\mu,9}$   | Fixed          | Turn movement (Left =1, else=0) | -0.129  | 0.080           | [-0.265, -0.061] <sup>†</sup>  | -0.579 | 0.310           | [-1.231, -0.220] <sup>†</sup> |
| <i>Scale Parameter (<math>\log \sigma_{k,i}</math>)</i> |                |                                 |         |                 |                                |        |                 |                               |
| $\beta_{\sigma,0}$                                      | Fixed          | Intercept                       | -0.100  | 0.038           | [-0.167, -0.009] <sup>†</sup>  | -      | -               | -                             |
| $\beta_{\sigma,0,k}$                                    | Random         | Intercept                       | -       | -               | -                              | -0.197 | 0.098           | [-0.374, -0.001] <sup>†</sup> |
| $\gamma_{\sigma,1,k}$                                   | Random         | Relative distance               | -       | -               | -                              | 0.042  | 0.034           | [-0.028, 0.107]               |
| $\beta_{\sigma,1}$                                      | Fixed          | Relative speed                  | 0.036   | 0.019           | [0.013, 0.063] <sup>†</sup>    | 0.040  | 0.019           | [0.001, 0.076] <sup>†</sup>   |
| $\beta_{\sigma,2}$                                      | Fixed          | Relative acceleration           | 0.012   | 0.015           | [-0.015, 0.042]                | 0.046  | 0.011           | [0.009, 0.084] <sup>†</sup>   |
| $\beta_{\sigma,3}$                                      | Fixed          | Relative deceleration           | -0.147  | 0.056           | [-0.285, -0.027] <sup>†g</sup> | -0.177 | 0.056           | [-0.289, -0.047] <sup>†</sup> |
| $\beta_{\sigma,4}$                                      | Fixed          | Relative distance               | 0.209   | 0.038           | [0.140, 0.282] <sup>†</sup>    | -      | -               | -                             |
| $\beta_{\sigma,5}$                                      | Fixed          | Jerk                            | 0.611   | 0.133           | [0.227, 0.886] <sup>†</sup>    | 0.109  | 0.033           | [0.016, 0.156] <sup>†</sup>   |
| $\beta_{\sigma,6}$                                      | Fixed          | Heading difference              | -0.023  | 0.018           | [-0.057, -0.004] <sup>†</sup>  | -0.090 | 0.021           | [-0.130, -0.049] <sup>†</sup> |
| $\beta_{\sigma,7}$                                      | Fixed          | Steering difference             | -0.012  | 0.018           | [-0.045, 0.023]                | -0.024 | 0.020           | [-0.062, -0.017] <sup>†</sup> |
| $\beta_{\sigma,8}$                                      | Fixed          | Volume                          | 0.004   | 0.016           | [-0.028, 0.034]                | 0.029  | 0.018           | [0.003, 0.064] <sup>†</sup>   |
| $\beta_{\sigma,9}$                                      | Fixed          | Turn movement (Left =1, else=0) | 0.100   | 0.053           | [0.019, 0.197] <sup>†</sup>    | 0.264  | 0.049           | [0.163, 0.349] <sup>†</sup>   |
| <i>Shape Parameter (<math>\xi_{k,i}</math>)</i>         |                |                                 |         |                 |                                |        |                 |                               |
| $\beta_{\xi,0}$   | Fixed          | Intercept                       | -0.677  | 0.042           | [-0.749, -0.594] <sup>†</sup>  | -      | -               | -                             |
| $\beta_{\xi,0,k}$                                       | Random         | Intercept                       | -       | -               | -                              | -0.680 | 0.096           | [-0.876, -0.501] <sup>†</sup> |
| <i>Model Fit</i>  |                |                                 |         |                 |                                |        |                 |                               |
| DIC   |                |                                 | 3197    |                 |                                | 3179.6 |                 |                               |
| WAIC  |                |                                 | 3202    |                 |                                | 3194.4 |                 |                               |
| LOOIC   |                |                                 | 3212.87 |                 |                                | 3209.8 |                 |                               |

HBSFP Hierarchical Bayesian Spatial Fixed Parameter  
HBSGRP Hierarchical Bayesian Spatial Grouped Random Parameter  
<sup>a</sup> Standard deviation  
<sup>b</sup> 95% Bayesian credible interval  
- Covariate not included in the model  
<sup>†</sup> Indicates statistical significance at the 95% level (interval excludes 0)

### 5.1.2. Segment-level

The HBSGRP model for segment-level V-V near misses introduces random parameters within a hierarchical structure (Table 7). Specifically, the intercept and three time-varying vehicle dynamics—relative speed, relative deceleration, and relative distance—were allowed to vary across segments (Fig. 11). This specification recognizes that longitudinal interactions in uninterrupted midblock contexts are shaped by both driver behavior and roadway characteristics (lane configuration, median type, driveway density). All remaining covariates—relative acceleration, jerk, heading and steering differences, traffic volume, lane attributes, and access density—were treated as fixed effects given their comparatively stable influence across segments. The HBSGRP model yields substantially better fit than the fixed-effect alternative, confirming the value of partial pooling for capturing heterogeneity across the nine directional segments.

For the location parameter ( $\mu$ ), the random effects reveal meaningful differences across segments that align with expected driving dynamics. Relative speed shows a consistently positive effect, confirming that faster closing speeds sharply reduce 2D-TTC and intensify near-miss severity. The magnitude of this effect, however, varies across roadway

contexts Fig. 11. Segments with uninterrupted high-speed flows (e.g., S11) show the strongest impacts, while access-rich segments (e.g., S6, S7, and S13) display wider credible intervals, reflecting greater variability in interactions. Relative deceleration carries a negative sign overall, but its effect is less stable, suggesting that braking sometimes helps dissipate conflicts in smoother-flow environments, whereas in higher-speed segments the same braking often signals critical near-miss events. Relative distance exhibits a consistently negative association, indicating that shorter headways reliably elevate severity by restricting the available buffer for evasive maneuvers. The posterior variation across segments suggests that spacing behavior differs between divided and undivided facilities. Finally, in some segments with sparse block maxima samples, the intercept's credible intervals approach zero, highlighting weaker estimation stability under limited data conditions.

Among the fixed effects, relative acceleration shows a significant negative association with  $\mu$ , indicating that acceleration phases are systematically linked to more severe near-misses on segments. This pattern contrasts with intersections, where acceleration often reflects flow resumption under green signals. Along segments, however, aggressive acceleration during overtaking or merging reduces spacing and elevates risk. Jerk also exhibits a negative effect, underscoring how abrupt longitudinal control contributes to critical outcomes. Lateral control indicators—heading and steering differences—display positive coefficients, suggesting that lateral adjustments provide modest increases in 2D-TTC where lane-changing flexibility is available. Driveway density is positively associated with  $\mu$ , a result that may seem counterintuitive but likely reflects anticipatory caution by drivers in access-rich environments. In contrast, undivided medians show a strong negative effect, confirming that exposure to opposing traffic flows produces consistently more severe interactions.

For the scale parameter ( $\sigma$ ), the random effects for relative speed, deceleration, and distance are all negative, indicating that extreme longitudinal dynamics compress outcome variability and yield uniformly critical near-miss conditions. This pattern is evident in Fig. 11, where high-speed and short-spacing conditions cluster tightly around lower 2D-TTC values, producing narrow posteriors in segments such as S12 and S15. By contrast, segments like S10 display wider credible intervals, reflecting weaker estimation stability under sparse BM samples. Among the fixed effects, jerk and heading difference increase  $\sigma$ , suggesting that volatile acceleration or lateral corrections introduce greater heterogeneity in near-miss outcomes. In contrast, lane number and lane width reduce  $\sigma$ , implying that additional maneuvering space fosters more predictable interactions. Driveway density increases dispersion, consistent with the variability created by frequent merging and crossing maneuvers. Median type again shows a strong negative effect, reinforcing that undivided facilities compress severity outcomes into consistently critical ranges.

Finally, the shape parameter ( $\xi$ ) remains negative and statistically significant across segment groups, confirming a bounded upper tail consistent with the Weibull domain. This finding indicates physical and behavioral constraints on extreme near-miss severity, governed by speed environment, roadway geometry, and driver reaction capacity. Overall, the segment-level results emphasize the central role of longitudinal dynamics—acceleration, braking, and headway—in determining near-miss severity, while roadway features such as medians, lane width, and access density primarily shape variability. The strong performance of the HBSGRP model underscores its value in capturing these segment-specific dynamics, which fixed-parameter structures fail to represent, particularly in accounting for the spatially contingent effects of speed and spacing in midblock contexts.

The HBSGRP model for segment-level V-I near-misses offers insights into how longitudinal dynamics and roadway design jointly shape the severity and variability of extreme 2D-TTC outcomes (Table 8, Fig. 12). In this model, the intercept and relative distance are specified as group-level random effects in both the location and scale components, capturing spatial heterogeneity in how spacing influences near-miss severity across segments. All other covariates, including relative speed, acceleration, deceleration, jerk, heading difference, steering angle difference, traffic volume, lane attributes, driveway density, median type, and left-lane presence—are modeled as fixed effects to represent their more consistent contributions across segment environments.

For the location parameter, reduced clearance to roadway boundaries exerts a strong negative effect on 2D-TTC, confirming that closer spacing to infrastructure consistently produces more critical near-miss outcomes. The random effect for distance further indicates that this influence varies across segment groups, reflecting sensitivity to local geometric and operational conditions such as median presence or driveway density. Relative speed shows a notable divergence: while the fixed-parameter model suggests higher speeds intensify severity, the grouped specification produces a small positive estimate, implying that in some contexts faster travel may coincide with greater clearance from boundaries (e.g., drivers maintaining lane center on free-flow arterials). This reversal highlights how heterogeneous speed environments fundamentally alter the role of speed in shaping V-I severity. Relative acceleration is positive and significant, suggesting that acceleration phases often represent clearance from roadside constraints (e.g.,

moving away from curbs or barriers) rather than heightened risk. By contrast, relative deceleration retains a negative effect across both models, indicating that braking near boundaries is typically associated with abrupt evasive actions, sharply reducing 2D-TTC and producing more critical near-miss conditions.

Several geometric and operational features also shape V-I near-miss severity at the segment level. Heading and steering differences exhibit significant positive coefficients, indicating that lateral adjustments toward or away from boundaries provide modest clearance gains and mitigate severity. Traffic volume, lane number, and lane width also emerge as positive contributors in the HBSGRP specification, suggesting that wider, higher-capacity segments allow greater separation from roadside features, producing slightly larger 2D-TTC values. The effect of driveway density, however, is particularly notable: while insignificant in the fixed-parameter model, the grouped specification yields a large negative estimate with a wide CI. This suggests that dense roadside access points intensify boundary conflicts by forcing frequent merging and turning maneuvers, though the data remain sensitive to localized characteristics. Median type is also significant, with undivided facilities consistently producing lower 2D-TTC values, reflecting heightened exposure to opposing flows and limited recovery space near boundaries. The left-lane variable shows a sign reversal, with the fixed model suggesting higher severity in interior lanes and the grouped model indicating greater severity in outer lanes. This pattern highlights heterogeneity across segment groups, where lane position relative to curbs, medians, or roadside access alters the likelihood of boundary-related near misses.

The scale parameter provides complementary insights into the variability of boundary-related near misses. The random effect for relative distance is positive, indicating that reduced clearance to roadside features not only increases severity but also broadens variability, as drivers adopt divergent strategies when negotiating minimal spacing with curbs, medians, or barriers. Relative speed also shows a positive association with scale, suggesting that higher speeds amplify heterogeneity in boundary interactions—contrasting with V-V near misses, where speed reduces dispersion—because drivers respond differently to infrastructure proximity under fast-moving conditions. Acceleration, by contrast, has a negative coefficient in the grouped model, implying that acceleration phases near boundaries often reflect smoother clearance maneuvers, yielding more predictable outcomes. Relative deceleration also reduces variability, indicating that braking close to infrastructure compresses outcomes into uniformly critical events.

Geometric attributes further shape variability. Lane width exerts a positive effect, showing that while wider lanes provide greater average clearance, they also increase variability by enabling a broader range of lateral positioning relative to boundaries. The undivided median type strongly increases scale, underscoring that the absence of a raised median not only heightens risk but also expands outcome variability due to heterogeneous driver avoidance maneuvers. The left-lane variable is also positive, indicating that boundary proximity in outer lanes produces more heterogeneous near-miss outcomes compared to interior lanes. Finally, driveway density, though statistically unstable, suggests that variability is strongly site-dependent, as frequent access points create unpredictable driver–infrastructure interactions.

The shape parameter remains negative and significant across both specifications, confirming that the upper tail of the 2D-TTC distribution is bounded. This supports the Weibull domain for extremes and indicates that even in V-I segment interactions, physical and behavioral limits constrain how severe the most critical boundary-related near-misses can become. Variation in the shape parameter across segment groups underscores the role of local geometry, access density, and operational conditions in shaping the extremal behavior of these events.

Segment-level analyses show that roadway geometry and vehicle dynamics jointly shape near-miss severity and variability. For V-V events, relative speed and distance dominate—speed amplifies severity while distance compresses variability, producing more deterministic outcomes under close-following conditions. For V-I events, the effect of speed is heterogeneous, sometimes reducing severity when clearance to boundaries is maintained, but elevating it when high speeds bring vehicles closer to curbs or medians. Access-related factors, particularly driveway density and median type, are critical for V-I outcomes, underscoring the role of access management and median design in roadside safety. Across both interaction types, the negative shape parameter indicates bounded extremes, reflecting physical and behavioral limits on crash risk escalation.

## 6. Model validation

The study corridor dataset provided precise geolocation for each extreme near-miss event (Eqn. 32) along with annual corridor-wide crash totals. Although annual crash data offer a useful aggregate benchmark, they lack precise geolocation of individual crashes and therefore cannot be directly matched to near-miss predictions at the event level. To address this limitation, validation was instead designed as an event-level case–control exercise, assessing whether

the model assigns higher exceedance probabilities to more severe near-miss events. Posterior exceedance probabilities were computed (Eqn. 30) across severity thresholds from  $-0.1$  to  $-0.9$  seconds, and classification performance was evaluated using ROC–AUC, a threshold-independent metric well suited to rare-event prediction.

ROC curves were generated for the four HBSGRP–UGEV variants, covering both V–V and V–I interactions at the segment and intersection levels. The results (Figure 13) reveal clear distinctions across near-miss types and roadway contexts. The V–V segment model achieved the highest predictive accuracy ( $AUC \approx 0.89$ ), reflecting the influence of dynamic variability in driver behavior. Relative speed, deceleration, and distance emerged as significant random parameters, capturing heterogeneity in conflict severity across segments. At the same time, fixed effects such as heading difference, steering difference, jerk, lane width, and driveway density contributed additional explanatory power, indicating that both dynamic interactions and roadway design shape V–V near-miss risks. The V–I model at the segment level achieved moderately strong accuracy ( $AUC \approx 0.79$ ) but displayed greater sensitivity to severity thresholds. Only relative distance emerged as a significant random parameter, while other vehicle dynamics (e.g., speed, deceleration, etc.) and roadway features (e.g., lane width, driveway density, median type, and etc.) contributed as fixed effects. This suggests that V–I risks are shaped primarily by localized conditions, with dynamic variability playing a comparatively smaller role than in V–V interactions.

At intersections, the V–V model achieved moderately strong accuracy ( $AUC \approx 0.82$ ) with low threshold sensitivity. Random parameters for relative speed and relative distance captured cross-location heterogeneity in approach and gap-acceptance conditions, while fixed effects—including deceleration/acceleration, steering and heading differences, jerk, and a left-turn indicator—explained lateral maneuvering and control effects. Together, these terms allow the model to represent both longitudinal and lateral conflict dynamics under signalized conditions, yielding stable performance. In contrast, the intersection-level V–I model performed weakest ( $AUC \approx 0.75$ ) and showing large fluctuations across thresholds, which reflects the complexity of boundary-related near-misses in intersections where turning trajectories, curb proximity, traffic signals, and pedestrian activity all interact.

Taken together, the results demonstrate that the HBSGRP–UGEV framework yields robust and consistent predictive accuracy for V–V interactions, particularly along corridor segments, where conflict dynamics are more regular and less influenced by intersectional variability. By contrast, V–I models—especially at intersections—showed lower stability and greater sensitivity to threshold specification, reflecting the complexity of boundary-related near-miss shaped by turning flows, curb geometry, and multimodal activity. These findings suggest that segment-level V–V estimates are the most operationally reliable for proactive monitoring, while intersection-level V–I models may require further refinement. Incorporating richer representations of curb design, pedestrian exposure, and high-resolution V–I proximity measures could strengthen stability and predictive performance in future applications.

## 7. Summary and conclusions

This study addresses the persistent challenge of estimating short-term crash occurrence risk (COR) in urban corridor-wide traffic environments, where conventional surrogate safety models often overlook detailed vehicle geometry, roadway context, and site-specific behavioral variability. Existing approaches have typically focused on vehicle–vehicle (V–V) interactions and neglected vehicle–infrastructure (V–I) conflicts, limiting their applicability at the corridor scale. To overcome these gaps, we introduced a geometry-aware two-dimensional time-to-collision (2D-TTC) indicator that incorporates vehicle dimensions, dynamic states, and roadway boundaries, enabling the detection of extreme near-miss events from both V–V and V–I interactions.

Extreme events were modeled through a nonstationary Univariate Generalized Extreme Value (UGEV) distribution embedded within a Hierarchical Bayesian Spatial Grouped Random Parameter (HBSGRP) framework. This structure allowed partial pooling across intersections and directional segments while preserving local heterogeneity, addressing data sparsity and contextual variation. High-resolution vehicle trajectories from the Argoverse-2 dataset were integrated with HD maps to extract near-miss events. Vehicle dynamics (relative speed, acceleration, deceleration, jerk, heading and steering differences, and traffic volume) and roadway features (lane width, driveway density, median type, turning movements, and lane position) were incorporated as covariates, with grouped random parameters specified for key dynamic variables. Grouped random parameters were specified for temporally varying dynamics, relative speed, relative deceleration, and relative distance, to capture their context-dependent effects. For benchmarking, a baseline hierarchical Bayesian fixed-parameter (HBSFP) model was also estimated.

Results showed that the HBSGRP model consistently outperformed its fixed-parameter counterpart, yielding lower DIC, WAIC, and LOOIC values and demonstrating greater stability. Random-parameter vehicle dynamics revealed

that relative speed, deceleration, and distance dominated V–V near misses at the segment level, whereas only relative distance was significant for V–I near misses. At intersections, V–V near misses were dominated by relative speed and distance, while no dynamic variables were significant for V–I near misses. Fixed covariates such as heading difference, steering difference, lane width, driveway density, and median type also showed significant effects, demonstrating the ability of the model to capture both dynamic behaviors and roadway design influences.

Validation results further confirmed model credibility. ROC–AUC validation confirmed robust predictive accuracy, with V–V segment models performing best (AUC  $\approx$  0.89), followed by intersection V–V ( $\approx$  0.82)), while V–I models showed moderate performance ( $\approx$  0.79 for segments,  $\approx$  0.75 for intersections). These findings indicate that while V–V risks can be reliably modeled, V–I interactions, particularly at intersections, remain more variable and complex.

While the proposed framework advances corridor-wide COR modeling, several aspects warrant further development. First, reliance on AV onboard sensors may introduce measurement bias in traffic state estimation and near-miss detection. Second, the 2D-TTC formulation simplifies nonlinear vehicle dynamics, which could understate risks during extreme evasive maneuvers. Third, the framework does not yet capture near-miss severity stratification. Future research offers opportunities to enrich this framework. Extending it to multivariate HBSGRP-UGEV models with complementary surrogate measures such as post-collision velocity change ( $\Delta V$ ) would provide deeper insights into crash severity dynamics. Incorporating vulnerable road user (VRU) near-misses, validating across diverse urban networks, calibrating for transferability, and benchmarking against GPD methods will further enhance robustness and generalizability. As AV deployment expands, increasingly rich trajectory datasets will strengthen the statistical power of HBSGRP-UGEV and open new opportunities for nuanced, multimodal safety assessments. Within this evolving data landscape, the proposed framework provides a scalable and adaptable foundation for proactive corridor-wide safety monitoring. By enabling early identification of high-risk conditions and supporting real-time traffic management, the framework aligns with the broader Vision Zero agenda, advancing the long-term goal of safer, more efficient, and equitable urban mobility.

**Acknowledgement:** This research is funded by Federal Highway Administration (FHWA) Exploratory Advanced Research 693JJ323C000010. The results do not reflect FHWA's opinions.

**Disclaimer:** The results presented in this document do not necessarily reflect those from the Federal Highway Administration.

**Data availability:** Data and code will be made available on reasonable request.

## CRedit authorship contribution statement

**Mohammad Anis:** Conceptualization, Methodology, Writing – original draft, Software, Writing – review & editing. **Yang Zhou:** Conceptualization, Methodology, Writing – review & editing, Supervision. **Dominique Lord:** Conceptualization, Methodology, Writing – review & editing, Supervision.

## References

- Ali, Y., Haque, M.M., Mannering, F., 2023a. Assessing traffic conflict/crash relationships with extreme value theory: Recent developments and future directions for connected and autonomous vehicle and highway safety research. *Analytic methods in accident research*, 100276.
- Ali, Y., Haque, M.M., Zheng, Z., 2022. An extreme value theory approach to estimate crash risk during mandatory lane-changing in a connected environment. *Analytic methods in accident research* 33, 100193.
- Ali, Y., Washington, S., Haque, M.M., 2023b. Estimating real-time crash risk at signalized intersections: A bayesian generalized extreme value approach. *Safety Science* 164, 106181.
- Allen, B.L., Shin, B.T., Cooper, P.J., 1978. Analysis of traffic conflicts and collisions. Technical Report. New Astron.
- Alozi, A.R., Hussein, M., 2022. Evaluating the safety of autonomous vehicle–pedestrian interactions: An extreme value theory approach. *Analytic methods in accident research* 35, 100230.
- Anis, M., Geedipally, S.R., Lord, D., 2025a. Pedestrian crash causation analysis near bus stops: Insights from random parameters negative binomial–lindley model. *Accident Analysis & Prevention* 220, 108137.
- Anis, M., Li, S., Geedipally, S.R., Zhou, Y., Lord, D., 2025b. Real-time risk estimation for active road safety: Leveraging waymo av sensor data with hierarchical bayesian extreme value models. *Accident Analysis & Prevention* 211, 107880.
- Arun, A., Haque, M.M., Bhaskar, A., Washington, S., Sayed, T., 2021. A systematic mapping review of surrogate safety assessment using traffic conflict techniques. *Accident Analysis & Prevention* 153, 106016.

- Blincoe, L., Miller, T., Wang, J.S., Swedler, D., Coughlin, T., Lawrence, B., Guo, F., Klauer, S., Dingus, T., 2023. The economic and societal impact of motor vehicle crashes, 2019 (Revised). Technical Report DOT HS 813 403. National Highway Traffic Safety Administration.
- Brooks, S.P., Gelman, A., 1998. General methods for monitoring convergence of iterative simulations. *Journal of computational and graphical statistics* 7, 434–455.
- Caesar, H., Bankiti, V., Lang, A.H., Vora, S., Liong, V.E., Xu, Q., Krishnan, A., Pan, Y., Baldan, G., Beijbom, O., 2020. nuscenec: A multimodal dataset for autonomous driving, in: *Proceedings of the IEEE/CVF conference on computer vision and pattern recognition*, pp. 11621–11631.
- Cai, Q., Abdel-Aty, M., Lee, J., Wang, L., Wang, X., 2018. Developing a grouped random parameters multivariate spatial model to explore zonal effects for segment and intersection crash modeling. *Analytic methods in accident research* 19, 1–15.
- Chen, J., Jönsson, P., Tamura, M., Gu, Z., Matsushita, B., Eklundh, L., 2004. A simple method for reconstructing a high-quality ndvi time-series data set based on the savitzky–golay filter. *Remote sensing of Environment* 91, 332–344.
- Choi, J., Chin, H., Park, H., Kwon, D., Baek, D., Lee, S.H., 2024. Safe and efficient trajectory optimization for autonomous vehicles using b-spline with incremental path flattening. *IEEE Transactions on Intelligent Transportation Systems*.
- Coles, S., Bawa, J., Trenner, L., Dorazio, P., 2001. An introduction to statistical modeling of extreme values. volume 208. Springer.
- Cooley, D., Naveau, P., Jomelli, V., Rabatel, A., Grancher, D., 2006. A bayesian hierarchical extreme value model for lichenometry. *Environmetrics: The official journal of the International Environmetrics Society* 17, 555–574.
- Davis, G.A., Hourdos, J., Xiong, H., Chatterjee, I., 2011. Outline for a causal model of traffic conflicts and crashes. *Accident Analysis & Prevention* 43, 1907–1919.
- Desai, J., Li, H., Mathew, J.K., Cheng, Y.T., Habib, A., Bullock, D.M., 2021. Correlating hard-braking activity with crash occurrences on interstate construction projects in indiana. *Journal of big data analytics in transportation* 3, 27–41.
- Eilers, P.H., Marx, B.D., 1996. Flexible smoothing with b-splines and penalties. *Statistical science* 11, 89–121.
- El-Basyouny, K., Sayed, T., 2009. Urban arterial accident prediction models with spatial effects. *Transportation research record* 2102, 27–33.
- El-Basyouny, K., Sayed, T., 2012a. Measuring direct and indirect treatment effects using safety performance intervention functions. *Safety science* 50, 1125–1132.
- El-Basyouny, K., Sayed, T., 2012b. Measuring safety treatment effects using full bayes non-linear safety performance intervention functions. *Accident Analysis & Prevention* 45, 152–163.
- Ettinger, S., Cheng, S., Caine, B., Liu, C., Zhao, H., Pradhan, S., Chai, Y., Sapp, B., Qi, C.R., Zhou, Y., et al., 2021. Large scale interactive motion forecasting for autonomous driving: The waymo open motion dataset, in: *Proceedings of the IEEE/CVF International Conference on Computer Vision*, pp. 9710–9719.
- Fu, C., Sayed, T., 2021a. Comparison of threshold determination methods for the deceleration rate to avoid a crash (drac)-based crash estimation. *Accident Analysis & Prevention* 153, 106051.
- Fu, C., Sayed, T., 2021b. Multivariate bayesian hierarchical gaussian copula modeling of the non-stationary traffic conflict extremes for crash estimation. *Analytic methods in accident research* 29, 100154.
- Fu, C., Sayed, T., 2021c. Random parameters bayesian hierarchical modeling of traffic conflict extremes for crash estimation. *Accident Analysis & Prevention* 157, 106159.
- Fu, C., Sayed, T., 2022a. Bayesian dynamic extreme value modeling for conflict-based real-time safety analysis. *Analytic methods in accident research* 34, 100204.
- Fu, C., Sayed, T., 2022b. Random-parameter bayesian hierarchical extreme value modeling approach with heterogeneity in means and variances for traffic conflict-based crash estimation. *Journal of transportation engineering, Part A: Systems* 148, 04022056.
- Fu, C., Sayed, T., 2023. Identification of adequate sample size for conflict-based crash risk evaluation: an investigation using bayesian hierarchical extreme value theory models. *Analytic methods in accident research* 39, 100281.
- Geiger, A., Lenz, P., Stiller, C., Urtasun, R., 2013. Vision meets robotics: The kitti dataset. *The international journal of robotics research* 32, 1231–1237.
- Gelman, A., Rubin, D.B., 1992. Inference from iterative simulation using multiple sequences. *Statistical science* 7, 457–472.
- Ghoul, T., Sayed, T., 2025. Cyclist safety assessment using autonomous vehicles. *Accident Analysis & Prevention* 212, 107923.
- Gilbert, A., Petrovic, D., Pickering, J.E., Warwick, K., 2021. Multi-attribute decision making on mitigating a collision of an autonomous vehicle on motorways. *Expert Systems with Applications* 171, 114581.
- Guo, Y., Essa, M., Sayed, T., Haque, M.M., Washington, S., 2019. A comparison between simulated and field-measured conflicts for safety assessment of signalized intersections in australia. *Transportation research part C: emerging technologies* 101, 96–110.
- Hayward, J., 1971. Near misses as a measure of safety at urban intersections. *Pennsylvania Transportation and Traffic Safety Center*.
- Houston, J., Zuidhof, G., Bergamini, L., Ye, Y., Chen, L., Jain, A., Omari, S., Igloukov, V., Ondruska, P., 2021. One thousand and one hours: Self-driving motion prediction dataset, in: *Conference on Robot Learning*, PMLR. pp. 409–418.
- Hussain, F., Li, Y., Arun, A., Haque, M.M., 2022. A hybrid modelling framework of machine learning and extreme value theory for crash risk estimation using traffic conflicts. *Analytic methods in accident research* 36, 100248.
- Islam, A.M., Shirazi, M., Lord, D., 2023. Grouped random parameters negative binomial-lindley for accounting unobserved heterogeneity in crash data with preponderant zero observations. *Analytic methods in accident research* 37, 100255.
- Islam, Z., Abdel-Aty, M., Cai, Q., Yuan, J., 2021. Crash data augmentation using variational autoencoder. *Accident Analysis & Prevention* 151, 105950.
- Jun, J., Ogle, J., Guensler, R., 2007. Relationships between crash involvement and temporal-spatial driving behavior activity patterns: use of data for vehicles with global positioning systems. *Transportation Research Record* 2019, 246–255.
- Kamel, A., Sayed, T., 2024. Transferability of real-time evt safety models: an investigation using autonomous vehicles data. *Transportmetrica A: Transport Science*, 1–26.
- Kamel, A., Sayed, T., Fu, C., 2023. Real-time safety analysis using autonomous vehicle data: a bayesian hierarchical extreme value model. *Transportmetrica B: Transport Dynamics* 11, 826–846.

- Kamel, A., Sayed, T., Kamel, M., 2024. Real-time combined safety-mobility assessment using self-driving vehicles collected data. *Accident Analysis & Prevention* 199, 107513.
- Kar, P., Venthuruthiyil, S.P., Chunchu, M., 2023. Non-stationary crash risk modelling of powered two-wheelers using extreme value analysis of surrogate crash events. *Accident Analysis & Prevention* 183, 106973.
- Kar, P., Venthuruthiyil, S.P., Chunchu, M., 2024. Crash risk estimation of heavy commercial vehicles on horizontal curves in mountainous terrain using proactive safety method. *Accident Analysis & Prevention* 199, 107521.
- Kesten, R., Usman, M., Houston, J., Pandya, T., Nadhamuni, K., Ferreira, A., Yuan, M., Low, B., Jain, A., Ondruska, P., Omari, S., Shah, S., Kulkarni, A., Kazakova, A., Tao, C., Platinsky, L., Jiang, W., Shet, V., 2019. Lyft level 5 av dataset 2019. <https://level5.lyft.com/dataset/>.
- Kumar, A., Mudgal, A., 2024. Risk assessment of rear-end crashes by incorporating vehicular heterogeneity into bayesian hierarchical extreme value models. *Transportmetrica B: Transport Dynamics* 12, 2323058.
- Lanzaro, G., Sayed, T., Fu, C., 2023. A comparison of pedestrian behavior in interactions with autonomous and human-driven vehicles: An extreme value theory approach. *Transportation research part F: traffic psychology and behaviour* 99, 1–18.
- Lee, J., Abdel-Aty, M., Cai, Q., 2017. Intersection crash prediction modeling with macro-level data from various geographic units. *Accident Analysis & Prevention* 102, 213–226.
- Li, P., Abdel-Aty, M., Yuan, J., 2020. Real-time crash risk prediction on arterials based on lstm-cnn. *Accident Analysis & Prevention* 135, 105371.
- Li, S., Anis, M., Lord, D., Zhang, H., Zhou, Y., Ye, X., 2024. Beyond 1d and oversimplified kinematics: A generic analytical framework for surrogate safety measures. *Accident Analysis & Prevention* 204, 107649.
- Lord, D., Mannering, F., 2010. The statistical analysis of crash-frequency data: A review and assessment of methodological alternatives. *Transportation research part A: policy and practice* 44, 291–305.
- Lord, D., Qin, X., Geedipally, S.R., 2021. *Highway safety analytics and modeling*. Elsevier.
- Mahmud, S.S., Ferreira, L., Hoque, M.S., Tavassoli, A., 2017. Application of proximal surrogate indicators for safety evaluation: A review of recent developments and research needs. *IATSS research* 41, 153–163.
- Mannering, F., Bhat, C.R., Shankar, V., Abdel-Aty, M., 2020. Big data, traditional data and the tradeoffs between prediction and causality in highway-safety analysis. *Analytic methods in accident research* 25, 100113.
- Minderhoud, M.M., Bovy, P.H., 2001. Extended time-to-collision measures for road traffic safety assessment. *Accident Analysis & Prevention* 33, 89–97.
- National Center for Statistics and Analysis, 2025. Early estimate of motor vehicle traffic fatalities in 2024. *Traffic Safety Facts Crash•Stats Brief Statistical Summary DOT HS 813 710*. National Highway Traffic Safety Administration.
- Nazir, F., Ali, Y., Sharma, A., Zheng, Z., Haque, M.M., 2023. Car-following crash risk analysis in a connected environment: A bayesian non-stationary generalised extreme value model. *Analytic methods in accident research* 39, 100278.
- Orsini, F., Gecchele, G., Gastaldi, M., Rossi, R., 2019. Collision prediction in roundabouts: a comparative study of extreme value theory approaches. *Transportmetrica A: transport science* 15, 556–572.
- Orsini, F., Gecchele, G., Gastaldi, M., Rossi, R., 2020. Large-scale road safety evaluation using extreme value theory. *IET Intelligent Transport Systems* 14, 1004–1012.
- Ozbay, K., Yang, H., Bartin, B., Mudigonda, S., 2008. Derivation and validation of new simulation-based surrogate safety measure. *Transportation research record* 2083, 105–113.
- Pei, X., Wong, S., Sze, N.N., 2011. A joint-probability approach to crash prediction models. *Accident Analysis & Prevention* 43, 1160–1166.
- Perkins, S.R., Harris, J.L., (1967). Traffic conflict characteristics: Freeway curve and exit area f1, december, 1966. *TRB* .
- Singh, S., Ali, Y., Haque, M.M., 2024. A bayesian extreme value theory modelling framework to assess corridor-wide pedestrian safety using autonomous vehicle sensor data. *Accident Analysis & Prevention* 195, 107416.
- Singh, S., Ali, Y., Mannering, F., Haque, M.M., 2025. Autonomous vehicle sensor data and the estimation of network-wide spatiotemporal generalized extreme value models of rear-end injury-severity crash frequencies. *Analytic Methods in Accident Research* , 100390.
- Songchitruksa, P., Tarko, A.P., 2006. The extreme value theory approach to safety estimation. *Accident Analysis & Prevention* 38, 811–822.
- Spiegelhalter, D.J., Best, N.G., Carlin, B.P., Van Der Linde, A., 2002. Bayesian measures of model complexity and fit. *Journal of the royal statistical society: Series b (statistical methodology)* 64, 583–639.
- St-Aubin, P., Miranda-Moreno, L., Saunier, N., 2013. An automated surrogate safety analysis at protected highway ramps using cross-sectional and before–after video data. *Transportation Research Part C: Emerging Technologies* 36, 284–295.
- Sun, T., Segu, M., Postels, J., Wang, Y., Van Gool, L., Schiele, B., Tombari, F., Yu, F., 2022. Shift: a synthetic driving dataset for continuous multi-task domain adaptation, in: *Proceedings of the IEEE/CVF Conference on Computer Vision and Pattern Recognition*, pp. 21371–21382.
- Tahir, H.B., Haque, M.M., 2024. A non-stationary bivariate extreme value model to estimate real-time pedestrian crash risk by severity at signalized intersections using artificial intelligence-based video analytics. *Analytic Methods in Accident Research* 43, 100339.
- Tak, S., Kim, S., Yeo, H., 2015. Development of a deceleration-based surrogate safety measure for rear-end collision risk. *IEEE transactions on intelligent transportation systems* 16, 2435–2445.
- Tarko, A.P., 2012. Use of crash surrogates and exceedance statistics to estimate road safety. *Accident Analysis & Prevention* 45, 230–240.
- Tarko, A.P., 2018. Estimating the expected number of crashes with traffic conflicts and the lomax distribution—a theoretical and numerical exploration. *Accident Analysis & Prevention* 113, 63–73.
- Venturuthiyil, S.P., Chunchu, M., 2022. Anticipated collision time (act): A two-dimensional surrogate safety indicator for trajectory-based proactive safety assessment. *Transportation research part C: emerging technologies* 139, 103655.
- Wang, C., Xu, C., Xia, J., Qian, Z., Lu, L., 2018. A combined use of microscopic traffic simulation and extreme value methods for traffic safety evaluation. *Transportation Research Part C: Emerging Technologies* 90, 281–291.
- Wang, T., Kim, S., Wenxuan, J., Xie, E., Ge, C., Chen, J., Li, Z., Luo, P., 2024. Deepaccident: A motion and accident prediction benchmark for v2x autonomous driving, in: *Proceedings of the AAAI Conference on Artificial Intelligence*, pp. 5599–5606.

- Washington, S., Karlaftis, M.G., Mannering, F., Anastasopoulos, P., 2020. Statistical and econometric methods for transportation data analysis. Chapman and Hall/CRC.
- Wilson, B., Qi, W., Agarwal, T., Lambert, J., Singh, J., Khandelwal, S., Pan, B., Kumar, R., Hartnett, A., Pontes, J.K., et al., 2023. Argoverse 2: Next generation datasets for self-driving perception and forecasting. arXiv preprint arXiv:2301.00493 .
- Xu, R., Xiang, H., Xia, X., Han, X., Li, J., Ma, J., 2022. Opv2v: An open benchmark dataset and fusion pipeline for perception with vehicle-to-vehicle communication, in: 2022 International Conference on Robotics and Automation (ICRA), IEEE. pp. 2583–2589.
- Yu, H., Luo, Y., Shu, M., Huo, Y., Yang, Z., Shi, Y., Guo, Z., Li, H., Hu, X., Yuan, J., et al., 2022. Dair-v2x: A large-scale dataset for vehicle-infrastructure cooperative 3d object detection, in: Proceedings of the IEEE/CVF Conference on Computer Vision and Pattern Recognition, pp. 21361–21370.
- Yuan, J., Abdel-Aty, M., Gong, Y., Cai, Q., 2019. Real-time crash risk prediction using long short-term memory recurrent neural network. Transportation research record 2673, 314–326.
- Zhang, H., Liptrott, M., Bessis, N., Cheng, J., 2019. Real-time traffic analysis using deep learning techniques and uav based video, in: 2019 16th IEEE International Conference on Advanced Video and Signal Based Surveillance (AVSS), IEEE. pp. 1–5.
- Zheng, L., Huang, Y., Sayed, T., Wen, C., 2021a. Validating the bayesian hierarchical extreme value model for traffic conflict-based crash estimation on freeway segments with site-level factors. Accident Analysis & Prevention 159, 106269.
- Zheng, L., Ismail, K., Meng, X., 2014. Freeway safety estimation using extreme value theory approaches: A comparative study. Accident Analysis & Prevention 62, 32–41.
- Zheng, L., Sayed, T., 2019. From univariate to bivariate extreme value models: Approaches to integrate traffic conflict indicators for crash estimation. Transportation research part C: emerging technologies 103, 211–225.
- Zheng, L., Sayed, T., 2020. A novel approach for real time crash prediction at signalized intersections. Transportation research part C: emerging technologies 117, 102683.
- Zheng, L., Sayed, T., Essa, M., 2019. Bayesian hierarchical modeling of the non-stationary traffic conflict extremes for crash estimation. Analytic methods in accident research 23, 100100.
- Zheng, L., Sayed, T., Mannering, F., 2021b. Modeling traffic conflicts for use in road safety analysis: A review of analytic methods and future directions. Analytic methods in accident research 29, 100142.

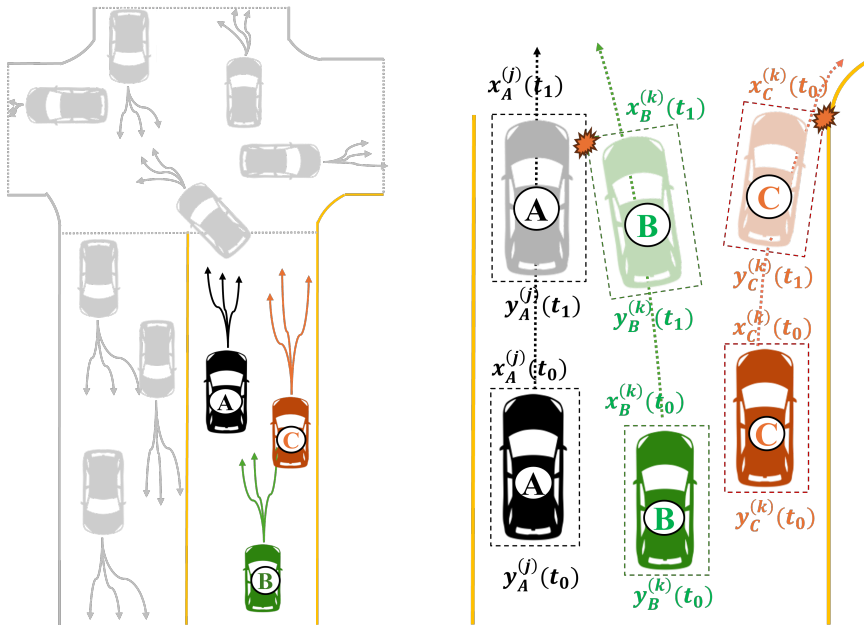


Fig. 1. Computation of 2D-TTC for near-miss scenarios

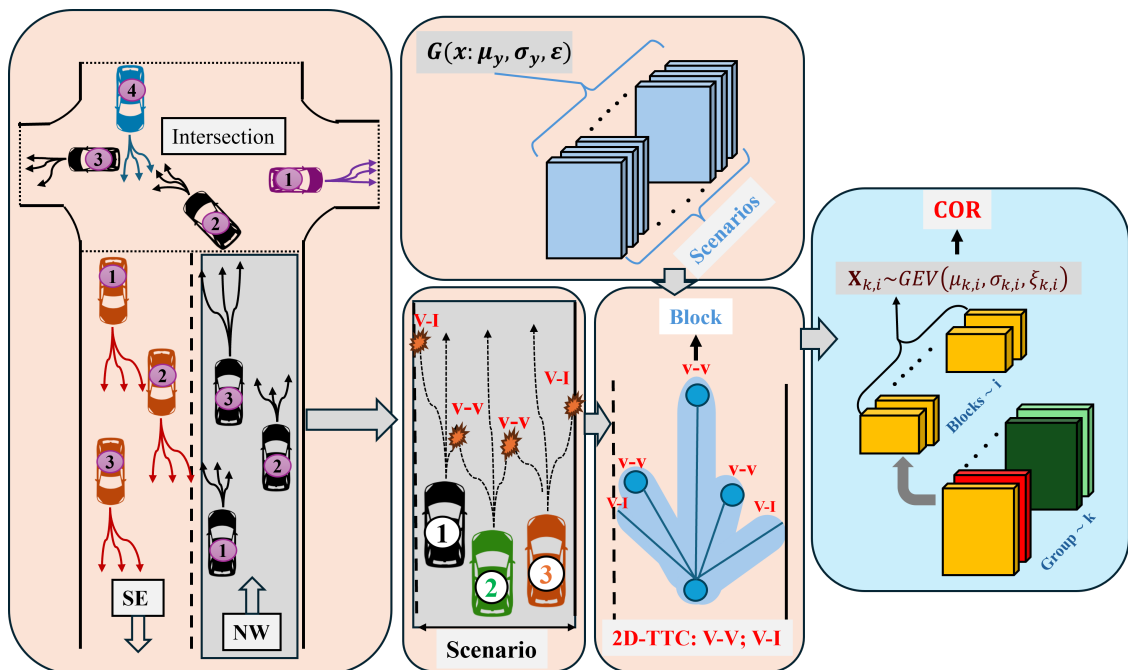
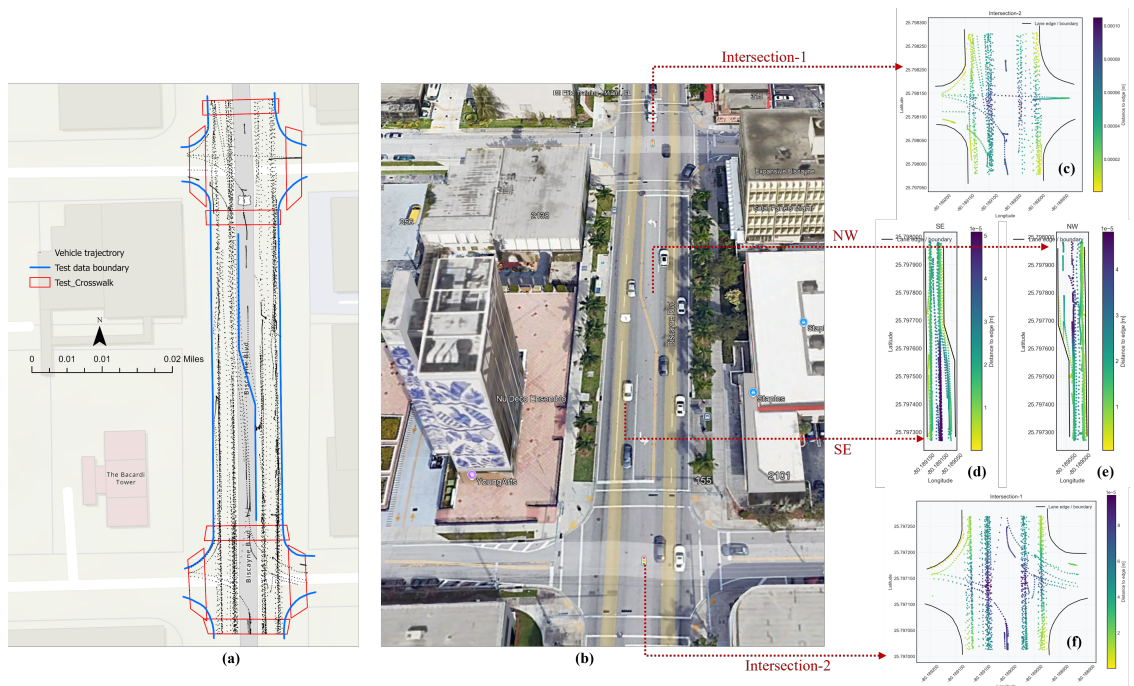
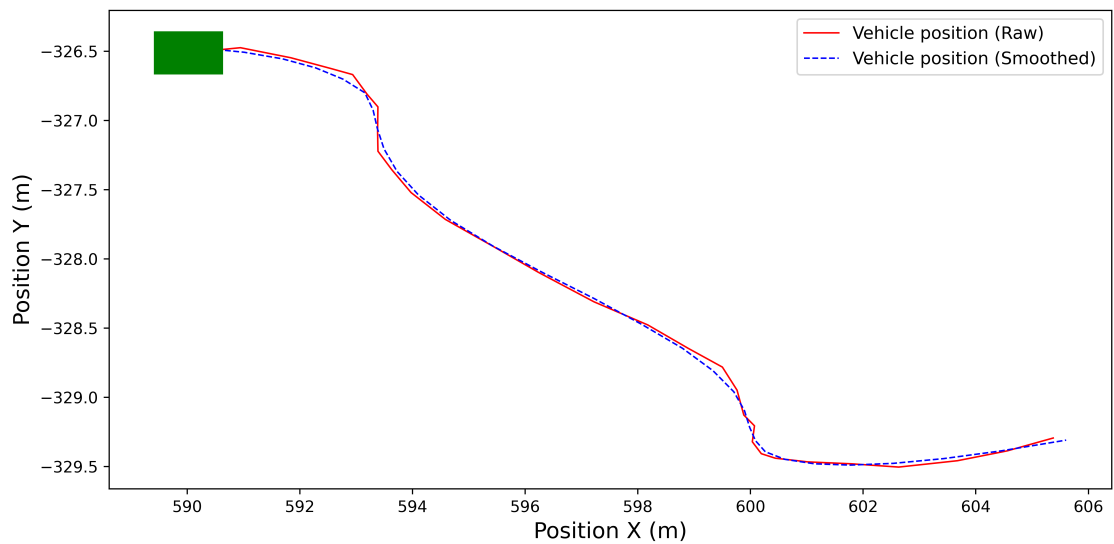


Fig. 2. COR time series generation



**Fig. 3.** AV data transformed to real-world coordinates and aligned: (a) trajectories with lane boundaries and crosswalks, (b) validation with satellite imagery, and (c–f) directional traffic patterns highlighting interaction hotspots.



**Fig. 4.** Effect of B-spline smoothing on a sample trajectory, showing removal of noise while preserving geometric fidelity

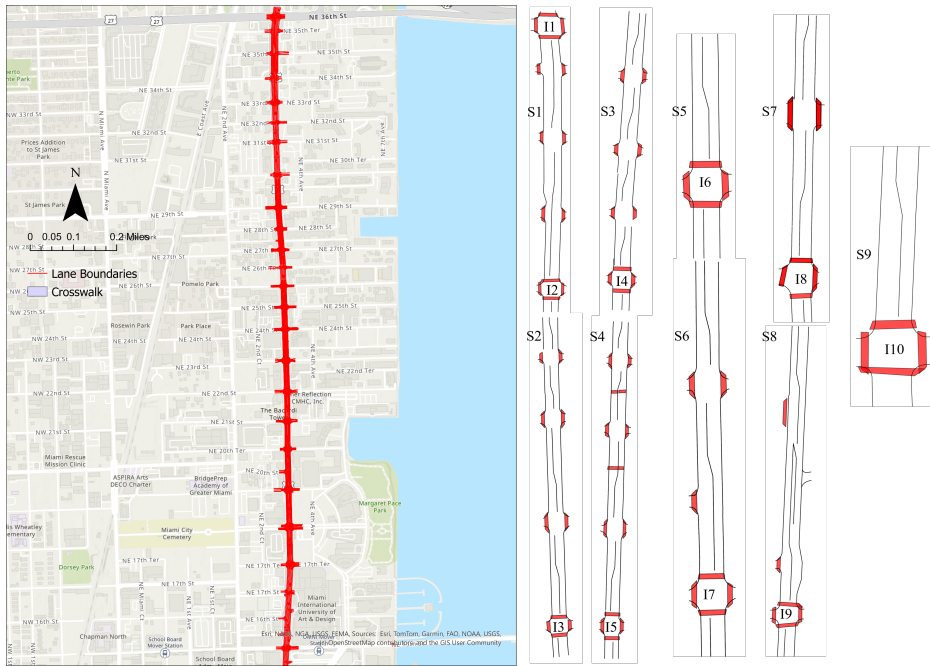


**Fig. 5.** Segmented study corridor along Biscayne Boulevard, Miami, with lane boundaries and crosswalks. Insets show direction-specific segments (S1–S9) and intersections (I1–I10)

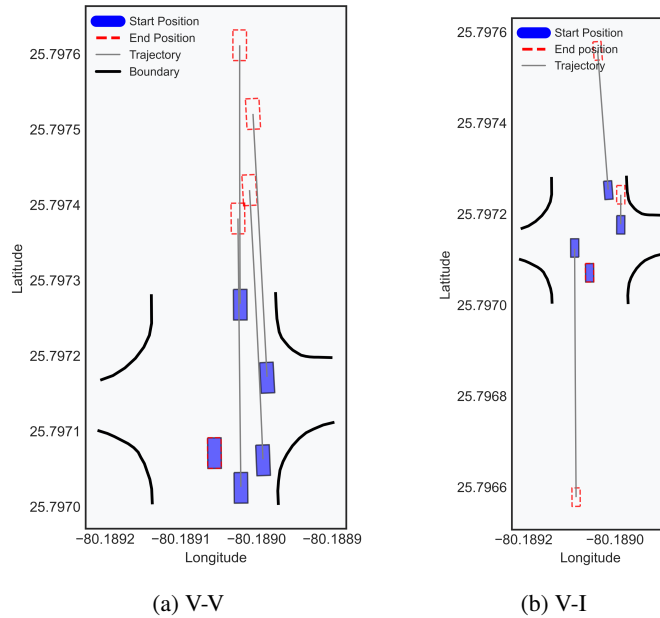


**Fig. 6.** Representative intersection-level near-miss detection using the 2D-TTC framework: (a) V–V and (b) V–I

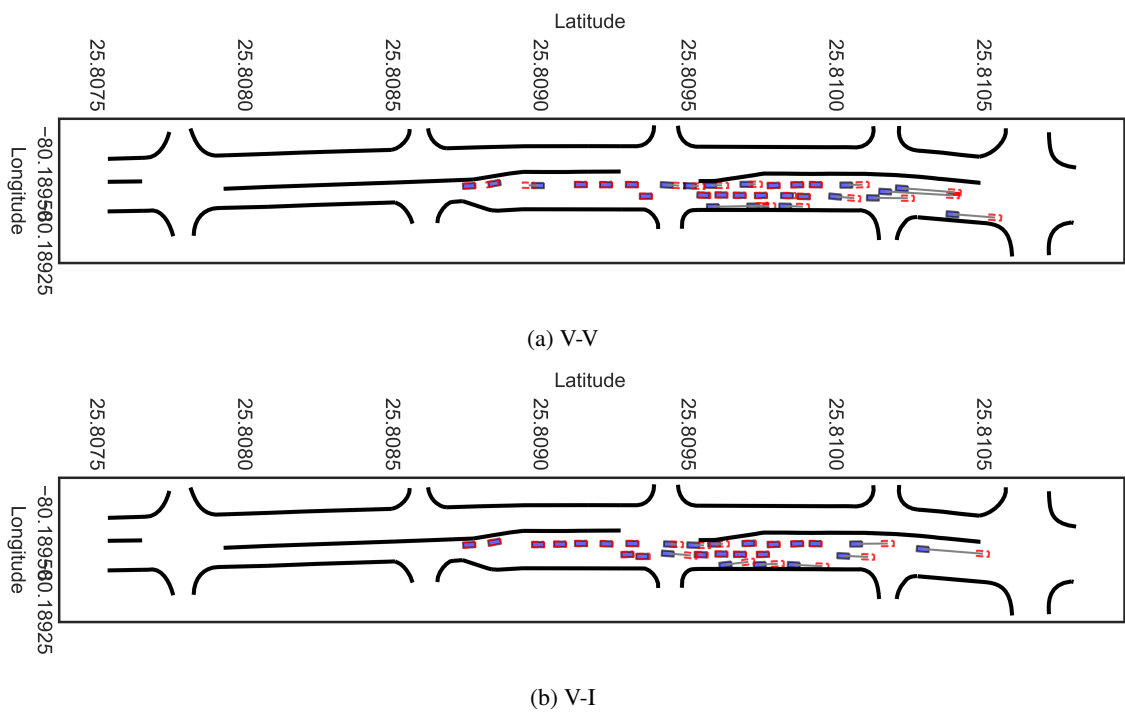
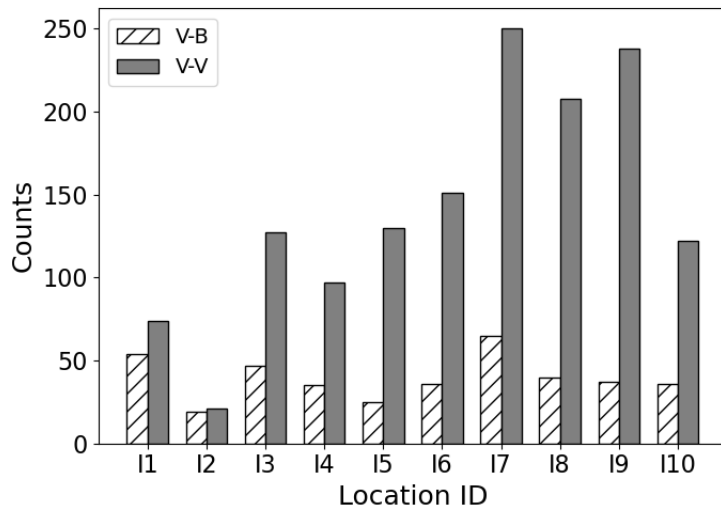
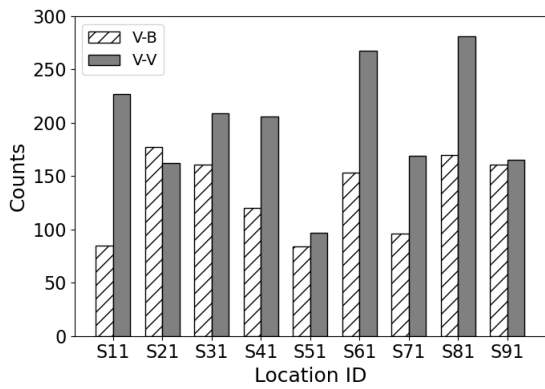


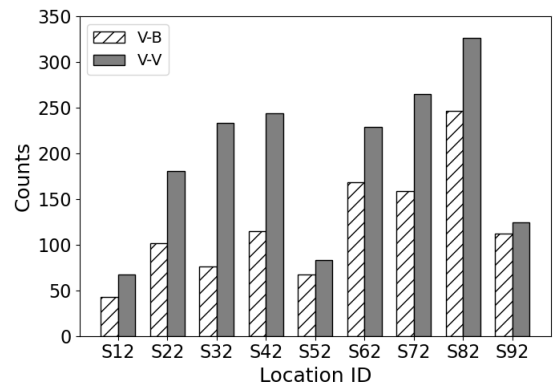
**Fig. 7.** Representative segment-level near-miss detection using the 2D-TTC framework: (a) V-V and (b) V-I



(a) Intersection



(b) Segment: NB



(c) Segment: SB

**Fig. 8.** BM near-miss frequencies by location type and direction

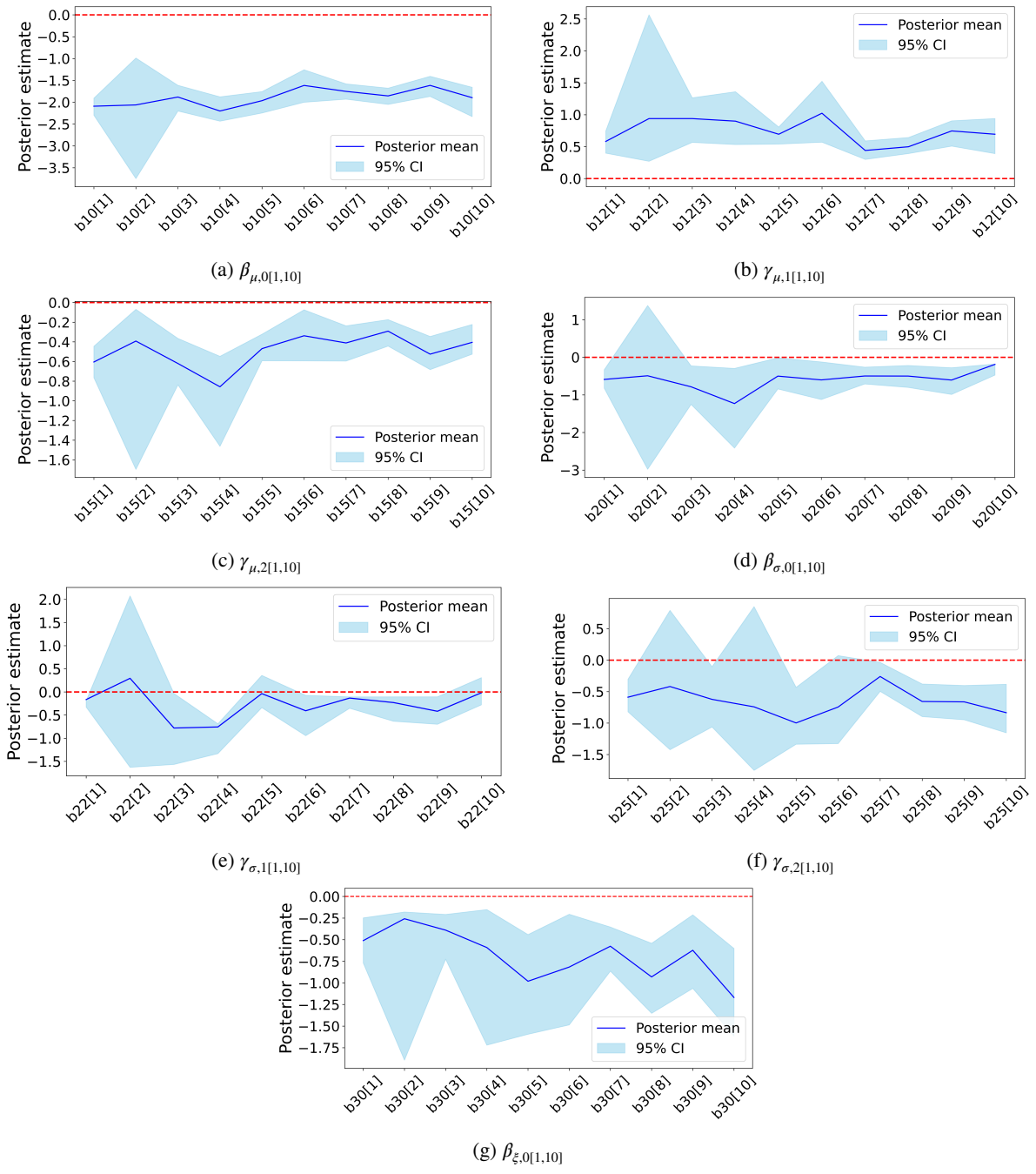


**Fig. 9.** Posterior estimates for V-V near-misses at intersections

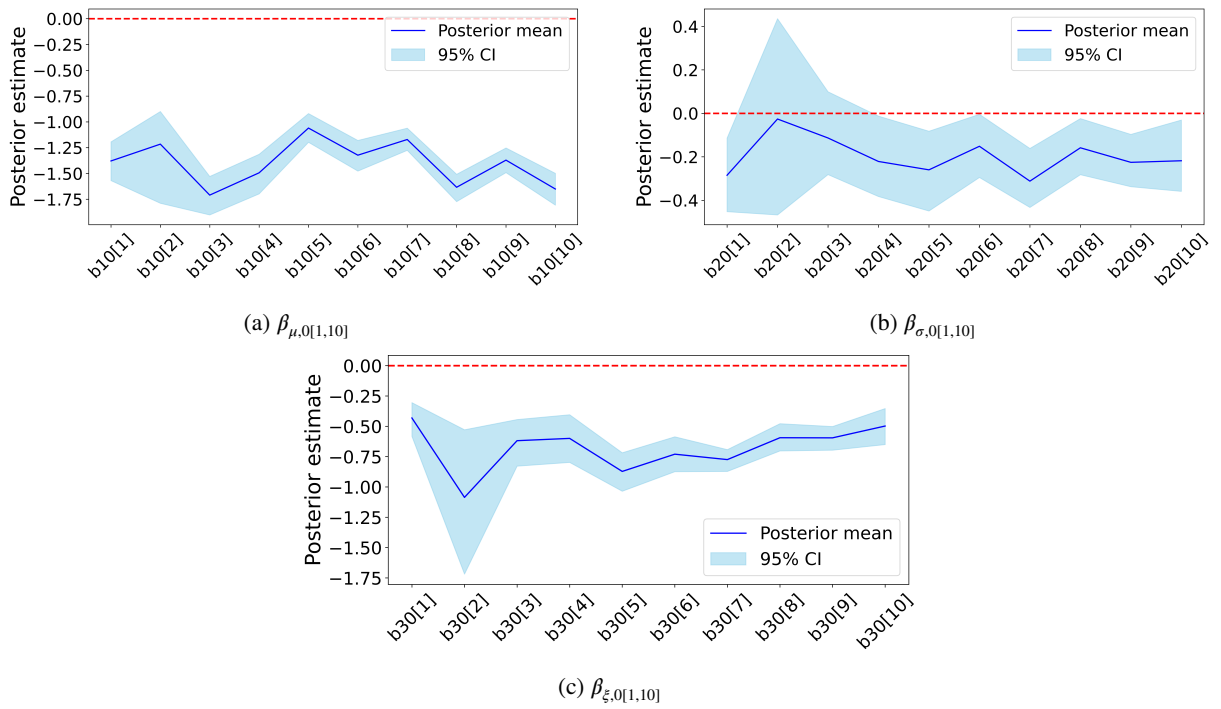


**Fig. 10.** Posterior estimates for V-I near-misses at intersections

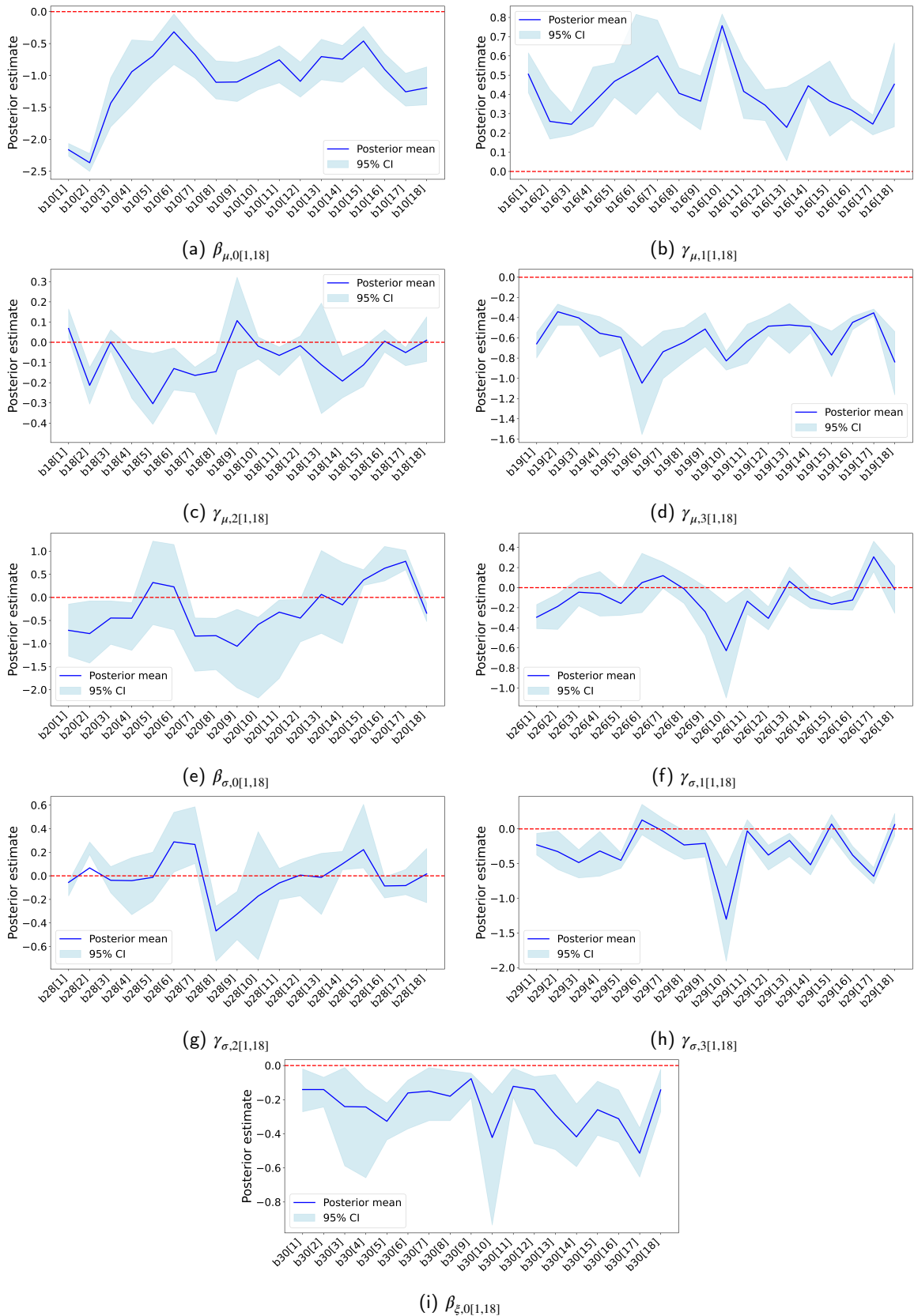


Fig. 11. Posterior estimates for V-V near-misses at segments

**Table 7**  
Posterior estimates V-V near misses at segments

| Model Parameters  | Hyperparameter | Covariate                              | HBSFP  |                 |                               | HBSGRP |                 |                               |
|---|----------------|--|--------|-----------------|-------------------------------|--------|-----------------|-------------------------------|
|   |                |  | Mean   | SD <sup>a</sup> | 95% CRI <sup>b</sup>          | Mean   | SD <sup>a</sup> | 95% CRI <sup>b</sup>          |
| <i>Location Parameter (<math>\mu_{k,i}</math>)</i>      |                |  |        |                 |                               |        |                 |                               |
| $\beta_{\mu,0}$   | Fixed          | Intercept                              | -2.117 | 0.032           | [-2.181, -2.025] <sup>†</sup> | -      | -               | -                             |
| $\beta_{\mu,0,k}$                                       | Random         | Intercept                              | -      | -               | -                             | -1.047 | 0.171           | [-1.369, -0.772] <sup>†</sup> |
| $\gamma_{\mu,1,k}$                                      | Random         | Relative speed                         | -      | -               | -                             | 0.406  | 0.068           | [0.286, 0.543] <sup>†</sup>   |
| $\gamma_{\mu,2,k}$                                      | Random         | Relative deceleration                  | -      | -               | -                             | -0.082 | 0.016           | [-0.197, -0.057] <sup>†</sup> |
| $\gamma_{\mu,3,k}$                                      | Random         | Relative distance                      | -      | -               | -                             | -0.600 | 0.082           | [-0.779, -0.454] <sup>†</sup> |
| $\beta_{\mu,1}$   | Fixed          | Relative speed                         | 0.446  | 0.037           | [0.376, 0.519] <sup>†</sup>   | -      | -               | -                             |
| $\beta_{\mu,2}$   | Fixed          | Relative acceleration                  | -0.068 | 0.017           | [-0.154, -0.034] <sup>†</sup> | -0.079 | 0.037           | [-0.163, -0.032] <sup>†</sup> |
| $\beta_{\mu,3}$   | Fixed          | Relative deceleration                  | -0.074 | 0.018           | [-0.108, -0.040] <sup>†</sup> | -      | -               | -                             |
| $\beta_{\mu,4}$   | Fixed          | Relative distance                      | -0.669 | 0.063           | [-0.801, -0.552] <sup>†</sup> | -      | -               | -                             |
| $\beta_{\mu,5}$   | Fixed          | Jerk                                   | -0.004 | 0.001           | [-0.007, -0.002] <sup>†</sup> | -0.156 | 0.043           | [-0.234, -0.101] <sup>†</sup> |
| $\beta_{\mu,6}$   | Fixed          | Heading difference                     | 0.043  | 0.016           | [0.011, 0.073] <sup>†</sup>   | 0.044  | 0.008           | [0.029, 0.059] <sup>†</sup>   |
| $\beta_{\mu,7}$   | Fixed          | Steering difference                    | 0.042  | 0.012           | [0.018, 0.066] <sup>†</sup>   | 0.026  | 0.010           | [0.007, 0.046] <sup>†</sup>   |
| $\beta_{\mu,8}$   | Fixed          | Volume                                 | 0.035  | 0.013           | [0.009, 0.060] <sup>†</sup>   | 0.019  | 0.008           | [0.002, 0.038] <sup>†</sup>   |
| $\beta_{\mu,9}$   | Fixed          | Lane no                                | -0.006 | 0.011           | [-0.027, 0.015]               | 0.009  | 0.011           | [-0.011, 0.032]               |
| $\beta_{\mu,10}$  | Fixed          | Lane width                             | 0.003  | 0.001           | [0.001, 0.007] <sup>†</sup>   | 0.017  | 0.009           | [0.002, 0.031] <sup>†</sup>   |
| $\beta_{\mu,11}$  | Fixed          | Driveway density                       | -0.001 | 0.015           | [-0.029, 0.027]               | 0.489  | 0.114           | [0.256, 0.578] <sup>†</sup>   |
| $\beta_{\mu,12}$  | Fixed          | Median (Undivided=1, else=0)           | -0.004 | 0.033           | [-0.070, 0.062]               | -0.412 | 0.155           | [-0.711, -0.070] <sup>†</sup> |
| $\beta_{\mu,13}$  | Fixed          | Vehicle position (Left lane=1, else=0) | 0.029  | 0.038           | [-0.048, 0.103]               | 0.055  | 0.006           | [0.012, 0.105] <sup>†</sup>   |
| <i>Scale Parameter (<math>\log \sigma_{k,i}</math>)</i> |                |  |        |                 |                               |        |                 |                               |
| $\beta_{\sigma,0}$                                      | Fixed          | Intercept                              | -0.622 | 0.045           | [-0.711, -0.533] <sup>†</sup> | -      | -               | -                             |
| $\beta_{\sigma,0,k}$                                    | Random         | Intercept                              | -      | -               | -                             | -0.253 | 0.047           | [-0.952, -0.156] <sup>†</sup> |
| $\gamma_{\sigma,1,k}$                                   | Random         | Relative speed                         | -      | -               | -                             | -0.055 | 0.026           | [-0.107, -0.003] <sup>†</sup> |
| $\gamma_{\sigma,2,k}$                                   | Random         | Relative deceleration                  | -      | -               | -                             | -0.119 | 0.018           | [-0.154, -0.084] <sup>†</sup> |
| $\gamma_{\sigma,3,k}$                                   | Random         | Relative distance                      | -      | -               | -                             | -0.304 | 0.117           | [-0.520, -0.084] <sup>†</sup> |
| $\beta_{\sigma,1}$                                      | Fixed          | Relative speed                         | -0.116 | 0.050           | [-0.217, -0.023] <sup>†</sup> | -      | -               | -                             |
| $\beta_{\sigma,2}$                                      | Fixed          | Relative acceleration                  | -0.611 | 0.097           | [-0.817, -0.439] <sup>†</sup> | -0.024 | 0.173           | [-0.277, 0.298]               |
| $\beta_{\sigma,3}$                                      | Fixed          | Relative deceleration                  | -0.060 | 0.019           | [-0.097, -0.024] <sup>†</sup> | -      | -               | -                             |
| $\beta_{\sigma,4}$                                      | Fixed          | Relative distance                      | 0.003  | 0.064           | [-0.121, 0.130]               | -      | -               | -                             |
| $\beta_{\sigma,5}$                                      | Fixed          | Jerk                                   | 0.006  | 0.000           | [0.004, 0.008] <sup>†</sup>   | 0.357  | 0.147           | [0.061, 0.611] <sup>†</sup>   |
| $\beta_{\sigma,6}$                                      | Fixed          | Heading difference                     | 0.065  | 0.017           | [0.032, 0.099] <sup>†</sup>   | 0.033  | 0.011           | [0.017, 0.068] <sup>†</sup>   |
| $\beta_{\sigma,7}$                                      | Fixed          | Steering difference                    | 0.011  | 0.016           | [-0.020, 0.043]               | -0.001 | 0.019           | [-0.031, 0.029]               |
| $\beta_{\sigma,8}$                                      | Fixed          | Volume                                 | -0.011 | 0.016           | [-0.043, 0.020]               | -0.012 | 0.015           | [-0.030, 0.029]               |
| $\beta_{\sigma,9}$                                      | Fixed          | Lane no                                | -0.031 | 0.014           | [-0.049, -0.005] <sup>†</sup> | -0.028 | 0.017           | [-0.061, -0.002] <sup>†</sup> |
| $\beta_{\sigma,10}$                                     | Fixed          | Lane width                             | -0.006 | 0.003           | [-0.012, -0.000] <sup>†</sup> | -0.015 | 0.009           | [-0.044, -0.001] <sup>†</sup> |
| $\beta_{\sigma,11}$                                     | Fixed          | Driveway density                       | 0.040  | 0.018           | [0.004, 0.075] <sup>†</sup>   | 0.284  | 0.215           | [0.019, 0.648] <sup>†</sup>   |
| $\beta_{\sigma,12}$                                     | Fixed          | Median (Undivided=1, else=0)           | 0.076  | 0.042           | [-0.006, 0.158]               | -0.205 | 0.095           | [-0.369, -0.058] <sup>†</sup> |
| $\beta_{\sigma,13}$                                     | Fixed          | Vehicle position (Left lane=1, else=0) | -0.049 | 0.052           | [-0.156, 0.051]               | -0.109 | 0.052           | [-0.209, -0.006] <sup>†</sup> |
| <i>Shape Parameter (<math>\xi_{k,i}</math>)</i>         |                |  |        |                 |                               |        |                 |                               |
| $\beta_{\xi,0}$   | Fixed          | Intercept                              | -0.116 | 0.030           | [-0.178, -0.059] <sup>†</sup> | -      | -               | -                             |
| $\beta_{\xi,0,k}$                                       | Random         | Intercept                              | -      | -               | -                             | -0.185 | 0.144           | [-0.436, -0.163] <sup>†</sup> |
| <i>Model Fit</i>  |                |  |        |                 |                               |        |                 |                               |
| DIC   |                |  |        | 4528            |                               |        | 4189            |                               |
| WAIC  |                |  |        | 4594            |                               |        | 4276            |                               |
| LOOIC   |                |  |        | 4608.25         |                               |        | 4278            |                               |

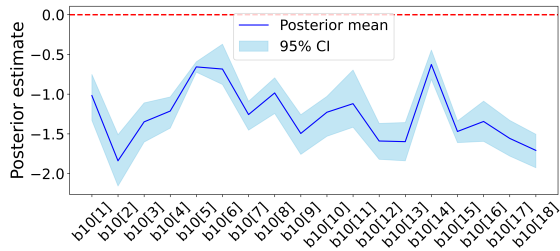
HBSFP Hierarchical Bayesian Spatial Fixed Parameter  
HBSGRP Hierarchical Bayesian Spatial Grouped Random Parameter

<sup>a</sup> Standard deviation

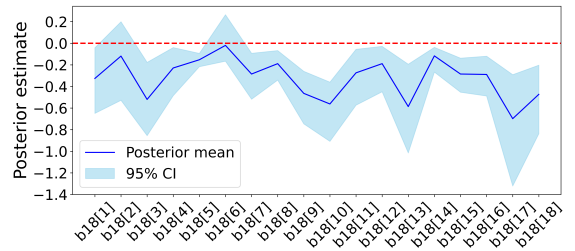
<sup>b</sup> 95% Bayesian credible interval

- Covariate not included in the model

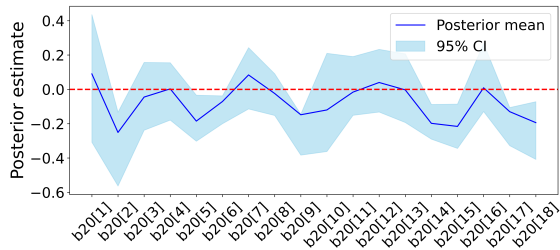
<sup>†</sup> Indicates statistical significance at the 95% level (interval excludes 0)



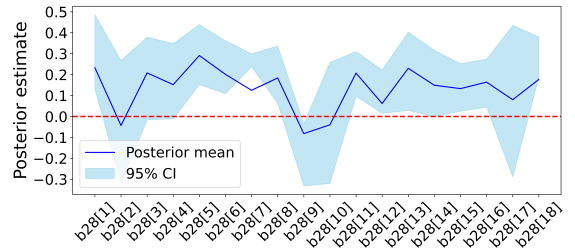
(a)  $\beta_{\mu,0[1,18]}$



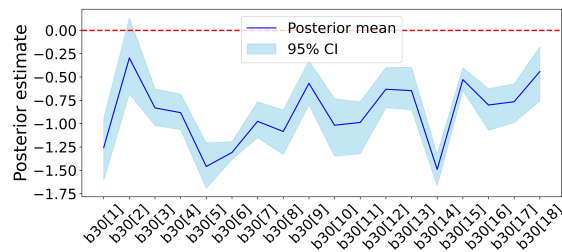
(b)  $\gamma_{\mu,1[1,18]}$



(c)  $\beta_{\sigma,0[1,18]}$



(d)  $\gamma_{\sigma,1[1,18]}$



(e)  $\beta_{\xi,0[1,18]}$

**Fig. 12.** Posterior estimates V-I near misses at segments

**Table 8**  
Posterior estimates V-I near misses at segments

| Model Parameters  | Hyperparameter | Covariate                              | HBSFP    |                 |                                | HBSGRP |                 |                               |
|---|----------------|--|----------|-----------------|--------------------------------|--------|-----------------|-------------------------------|
|   |                |  | Mean     | SD <sup>a</sup> | 95% CRI <sup>b</sup>           | Mean   | SD <sup>a</sup> | 95% CRI <sup>b</sup>          |
| <i>Location Parameter (<math>\mu_{k,i}</math>)</i>      |                |  |          |                 |                                |        |                 |                               |
| $\beta_{\mu,0}$   | Fixed          | Intercept                              | -1.287   | 0.037           | [-1.352, -1.22] <sup>†</sup>   | -      | -               | -                             |
| $\beta_{\mu,0,k}$                                       | Random         | Intercept                              | -        | -               | -                              | -1.263 | 0.122           | [-1.494, -1.037] <sup>†</sup> |
| $\gamma_{\mu,1,k}$                                      | Random         | Relative distance                      | -        | -               | -                              | -0.317 | 0.148           | [-0.632, -0.104] <sup>†</sup> |
| $\beta_{\mu,1}$   | Fixed          | Relative speed                         | -0.027   | 0.018           | [-0.061, -0.008] <sup>†</sup>  | 0.009  | 0.001           | [0.006, 0.027] <sup>†</sup>   |
| $\beta_{\mu,2}$   | Fixed          | Relative acceleration                  | 8.36E-04 | 0.019           | [-0.045, 0.036]                | 0.025  | 0.013           | [0.002, 0.057] <sup>†</sup>   |
| $\beta_{\mu,3}$   | Fixed          | Relative deceleration                  | -0.039   | 0.008           | [-0.098, -0.004] <sup>†</sup>  | -0.032 | 0.008           | [-0.087, -0.014] <sup>†</sup> |
| $\beta_{\mu,4}$   | Fixed          | Relative distance                      | -0.257   | 0.025           | [-0.304, -0.207] <sup>†</sup>  | -      | -               | -                             |
| $\beta_{\mu,5}$   | Fixed          | Jerk                                   | -0.124   | 0.069           | [-0.224, 0.289]                | -0.074 | 0.039           | [-0.124, 0.202]               |
| $\beta_{\mu,6}$   | Fixed          | Heading difference                     | 0.025    | 0.025           | [-0.025, 0.069]                | 0.027  | 0.014           | [0.001, 0.049] <sup>†</sup>   |
| $\beta_{\mu,7}$   | Fixed          | Steering difference                    | 0.033    | 0.017           | [0.004, 0.065] <sup>†</sup>    | 0.041  | 0.016           | [0.003, 0.066] <sup>†</sup>   |
| $\beta_{\mu,8}$   | Fixed          | Volume                                 | -0.002   | 0.007           | [-0.016, 0.010]                | 0.043  | 0.021           | [0.015, 0.084] <sup>†</sup>   |
| $\beta_{\mu,9}$   | Fixed          | Lane no                                | -0.001   | 0.012           | [-0.019, 0.016]                | 0.042  | 0.021           | [0.004, 0.078] <sup>†</sup>   |
| $\beta_{\mu,10}$  | Fixed          | Lane width                             | -0.027   | 0.018           | [-0.061, -0.008] <sup>†</sup>  | 0.013  | 0.009           | [0.000, 0.032] <sup>†</sup>   |
| $\beta_{\mu,11}$  | Fixed          | Driveway density                       | -0.007   | 0.024           | [-0.057, 0.042]                | -0.237 | 0.105           | [-0.403, -0.020] <sup>†</sup> |
| $\beta_{\mu,12}$  | Fixed          | Median (Undivided=1, else=0)           | -0.644   | 0.102           | [-0.773, -0.513] <sup>†</sup>  | -0.083 | 0.059           | [-0.196, -0.019] <sup>†</sup> |
| $\beta_{\mu,13}$  | Fixed          | Vehicle position (Left lane=1, else=0) | 0.057    | 0.033           | [0.028, 0.091] <sup>†</sup>    | -0.064 | 0.014           | [-0.082, -0.038] <sup>†</sup> |
| <i>Scale Parameter (<math>\log \sigma_{k,i}</math>)</i> |                |  |          |                 |                                |        |                 |                               |
| $\beta_{\sigma,0}$                                      | Fixed          | Intercept                              | -0.495   | 0.156           | [-0.703, -0.303] <sup>†</sup>  | -      | -               | -                             |
| $\beta_{\sigma,0,k}$                                    | Random         | Intercept                              | -        | -               | -                              | -0.076 | 0.104           | [-0.265, 0.083] <sup>†</sup>  |
| $\gamma_{\sigma,1,k}$                                   | Random         | Relative distance                      | -        | -               | -                              | 0.135  | 0.103           | [0.011, 0.318] <sup>†</sup>   |
| $\beta_{\sigma,1}$                                      | Fixed          | Relative speed                         | 0.039    | 0.016           | [0.012, 0.061] <sup>†</sup>    | 0.013  | 0.001           | [0.004, 0.038] <sup>†</sup>   |
| $\beta_{\sigma,2}$                                      | Fixed          | Relative acceleration                  | 0.002    | 0.017           | [-0.030, 0.042]                | -0.026 | 0.014           | [-0.064, -0.001] <sup>†</sup> |
| $\beta_{\sigma,3}$                                      | Fixed          | Relative deceleration                  | -0.036   | 0.013           | [-0.075, -0.014] <sup>†</sup>  | -0.048 | 0.021           | [-0.089, -0.022] <sup>†</sup> |
| $\beta_{\sigma,4}$                                      | Fixed          | Relative distance                      | 0.167    | 0.018           | [0.136, 0.199] <sup>†</sup>    | -      | -               | -                             |
| $\beta_{\sigma,5}$                                      | Fixed          | Jerk                                   | -0.108   | 0.054           | [0.452, -0.119]                | -0.078 | 0.119           | [-0.312, 0.078]               |
| $\beta_{\sigma,6}$                                      | Fixed          | Heading difference                     | -0.019   | 0.020           | [-0.053, 0.020]                | -0.029 | 0.017           | [-0.049, -0.001] <sup>†</sup> |
| $\beta_{\sigma,7}$                                      | Fixed          | Realative steering angle               | -0.033   | 0.012           | [-0.065, -0.001] <sup>†</sup>  | -0.032 | 0.024           | [-0.059, -0.003] <sup>†</sup> |
| $\beta_{\sigma,8}$                                      | Fixed          | Volume                                 | -0.007   | 0.018           | [-0.039, 0.027]                | 0.001  | 0.016           | [-0.026, 0.030]               |
| $\beta_{\sigma,9}$                                      | Fixed          | Lane no                                | -0.028   | 0.017           | [-0.058, -0.006] <sup>†</sup>  | -0.021 | 0.012           | [-0.046, -0.002] <sup>†</sup> |
| $\beta_{\sigma,10}$                                     | Fixed          | Lane width                             | -0.010   | 0.020           | [-0.044, 0.030]                | 0.018  | 0.016           | [0.010, 0.045] <sup>†</sup>   |
| $\beta_{\sigma,11}$                                     | Fixed          | Driveway density                       | 0.016    | 0.019           | [-0.021, 0.055]                | -0.125 | 0.028           | [-0.239, 0.018]               |
| $\beta_{\sigma,12}$                                     | Fixed          | Median (Undivided=1, else=0)           | 0.663    | 0.166           | [0.440, 0.880] <sup>†</sup>    | 0.174  | 0.090           | [0.263, 0.553] <sup>†</sup>   |
| $\beta_{\sigma,13}$                                     | Fixed          | Vehicle position (Left lane=1, else=0) | -0.046   | 0.027           | [-0.080, -0.012] <sup>†</sup>  | 0.055  | 0.010           | [0.039, 0.071] <sup>†</sup>   |
| <i>Shape Parameter (<math>\xi_{k,i}</math>)</i>         |                |  |          |                 |                                |        |                 |                               |
| $\beta_{\xi,0}$   | Fixed          | Intercept                              | -0.845   | 0.028           | [-0.897, -0.788] <sup>†g</sup> | -      | -               | -                             |
| $\beta_{\xi,0,k}$                                       | Random         | Intercept                              | -        | -               | -                              | -0.887 | 0.118           | [-1.123, -0.659] <sup>†</sup> |
| <i>Model Fit</i>  |                |  |          |                 |                                |        |                 |                               |
| DIC   |                |  | 6760     |                 |                                | 6550   |                 |                               |
| WAIC  |                |  | 6775     |                 |                                | 6595   |                 |                               |
| LOOIC   |                |  | 6791.2   |                 |                                | 6601   |                 |                               |

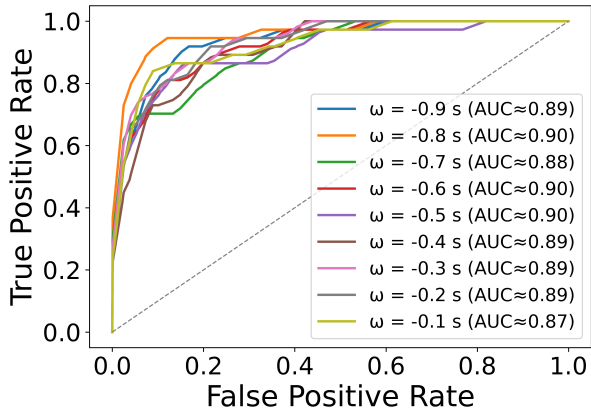
HBSFP Hierarchical Bayesian Spatial Fixed Parameter  
HBSGRP Hierarchical Bayesian Spatial Grouped Random Parameter

<sup>a</sup> Standard deviation

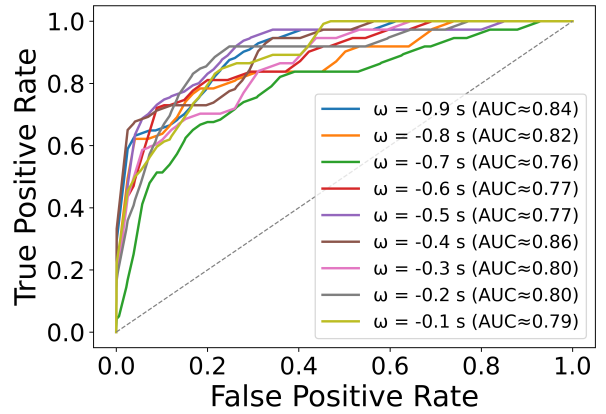
<sup>b</sup> 95% Bayesian credible interval

- Covariate not included in the model

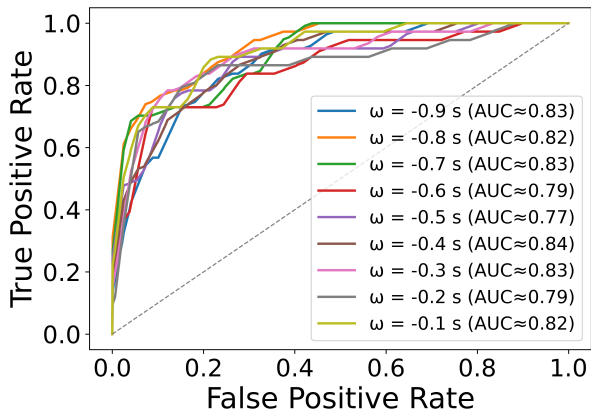
<sup>†</sup> Indicates statistical significance at the 95% level (interval excludes 0)



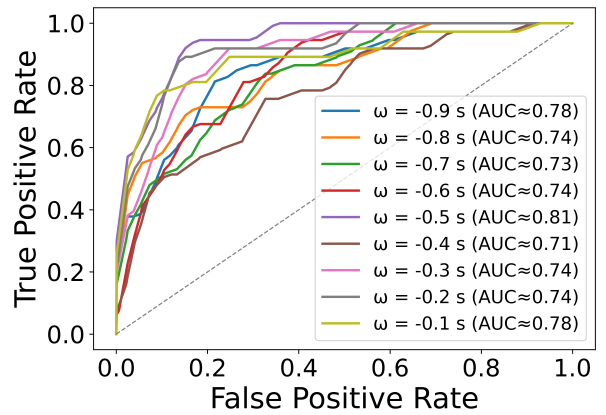
(a) V-V Segment



(b) V-I Segment



(c) V-V Intersection



(d) V-I Intersection

Fig. 13. ROC curves for four HBSGRP-UGEV models across severity thresholds from  $\omega = -0.1$ s to  $\omega = -0.9$ s